

**Hocam Merhaba,**

Son bir ay içerisinde, aşağıdaki tabloda başlıklarını verilen ve detayları alt sayfalarda sunulan üç makalemiz, uluslararası alan indekslerinde taranan dergiler tarafından kabul edilmiştir. Her bir makalenin tam metni ve kabul yazısı, ilgili makalenin sonunda yer almaktadır. Bu çalışmalar henüz DOI numarası olmadığı için puanlamaya dahil edilmemiştir.

Bunlara ek olarak, *Journal of the Mechanics and Physics of Solids* dergisine gönderdiğim ve yeni revizyonunu tamamladığım "*Stochastic Calibration of Biological Tissue Biomechanics: Bridging In-Vitro Measurements and In-Silico Simulations*" başlıklı çalışmayı da "Diğer Belgeler (Başvuru Belgeleri\_2\_Diğer Belgeler\_revised\_manuscript.pdf)" dosya adıyla sisteme ekledim. Sistem en fazla 15 MB dosya yüklemeye izin verdiginden, bu çalışmaya ait ek dosyalar (toplam 20.9 MB) bağlantı ([link](#)) şeklinde "Diğer Belgeler" bölümüne yüklenmiştir.

Saygılarımla,

Mahmut Pekedis, Ph.D.

Makale Adı	Dergi	Durum
Hip Prosthesis Design with a Shock Absorber	Gazi Journal of Engineering Sciences	Kabul edildi.
The Biaxial Tension-Compression Test Device for the Biomechanical Characterization of Soft Tissue	The Dokuz Eylül University Faculty of Engineering Journal of Science and Engineering	Kabul edildi.
Hector Slam Based Navigation with Integrated Object Detection	Uludağ University Journal of The Faculty of Engineering (UUJFE)	Kabul edildi.
Stochastic Calibration of Biological Tissue Biomechanics: Bridging In-Vitro Measurements and In-Silico Simulations	Journal of the Mechanics and Physics of Solids ( <a href="#">Tam metin</a> , <a href="#">ekler</a> )	Revizyon tamamlanmıştır. Karar aşamasındadır.

# GAZI

# JOURNAL OF ENGINEERING SCIENCES

## Hip Prosthesis Design with a Shock Absorber

Mert Narin<sup>a</sup>, Mahmut Pekedis<sup>\*b</sup>

Submitted: 07.03.2025 Revised : 24.05.2025 Accepted: 04.06.2025 doi:10.30855/gmbd.070525A04

<sup>a</sup>Ege University, Engineering Faculty, Dept. of Mechanical Engineering 35100 - İzmir, Türkiye, Orcid: 0009-0003-8878-2683

<sup>b</sup>Ege University, Engineering Faculty, Dept. of Mechanical Engineering 35100 - İzmir, Türkiye, Orcid: 0000-0002-3350-0277

\*Corresponding author: mahmut.pekedis@ege.edu.tr, mahmutpekedis@gmail.com

### ABSTRACT

**Keywords:** Hip prosthesis, shock absorber, finite element analysis

The conventional hip prostheses and the implanted bone are subjected to high stresses and strains under sudden and shock loadings (jumping, sudden movements, falling, etc.). In order to reduce these stresses and strains, we were inspired by a simple mechanical damper to design a hip prosthesis by incorporating a shock absorber proximally. Initially, hip prostheses with similar stem dimensions, Type A (conventional), Type B (spring based), and Type C (shock absorber based), were designed by considering prosthesis design parameters. Then, finite element analysis was performed for all three prostheses. Boundary conditions, such as physiological forces and fixations, were applied as suggested in studies reported in the literature. Once the simulations were completed, the time-dependent stress and deformation responses of the shock absorber-based and spring-based prostheses under sudden loading conditions were compared with those of the conventional prosthesis. The results showed that the stresses and strains in the shock absorber-based prosthesis were lower than those in both the spring-based and conventional prostheses. This finding suggests that the prosthesis could help reduce the frequency of revision arthroplasty surgeries.

### 1. Introduction

The mechanical functions of the lower extremity system largely depend on the biomechanical properties of various structures such as bones, joints, muscles, cartilage, ligaments, tendons, and soft tissues. Any damage, deterioration, or degeneration that may occur in these structures can lead to an imbalance within the system [1–3]. Major injuries such as fractures and dislocations, particularly in the hip joint, negatively affect individuals' mobility [4]. In cases where long-term treatments fail to yield satisfactory results, severe pain and irreversible loss of function may occur. When deformities are present in the pelvis and femur, total hip replacement surgery involving the femoral head and acetabulum is performed to help patients regain their ability to perform daily activities and improve their quality of life. In recent years, the increasing number of total hip arthroplasty procedures has been attributed particularly to the growing demand among younger age groups, who are observed to seek a return to active physical lifestyles following surgery. This rising demand has necessitated significant improvements beyond current innovations [5]. With the number of primary hip surgeries increasing each year worldwide, the number of revision hip surgeries is also expected to rise in the near future [6]. Therefore, the expected rise in revision surgeries and the increasing need for long-lasting prostheses have become significant concerns. Prostheses and implants are predominantly manufactured from metallic materials; however, due to their higher rigidity compared to bone, they may cause bone erosion and lead to complications [7]. As a result of these complications, loosening can occur at the bone–prosthesis interface. Aseptic loosening is defined as a separation occurring at the cement–bone interface or at the prosthesis–cement interface. The primary and most well-known causes of loosening include intense physical activity, errors in prosthesis positioning or design, and excessive body weight. The initial pain caused by aseptic loosening is typically felt in the thigh and groin regions under load-bearing conditions. It increases with intense physical activity and rotational movements of the hip. Additionally, during painful transitions from a seated to a standing position, patients may exhibit limb shortening or antalgic gait (a

compensatory gait pattern adopted to reduce pain) [8]. Overloading can weaken the bond between the cement and the bone, leading to implant loosening. Furthermore, if high stress concentrations develop in the connection areas of the prosthesis, they may result in long-term failure [9]. In the design of hip prostheses, criterias such as long service life, low stress, low deformation, and low wear levels are sought. In addition, the design is expected to enhance the product's durability and ensure consistent long-term performance [10]. After the hip prosthesis is designed, the more physiological the stress distribution profile is, the better the performance of the prosthesis will be in terms of function and durability [11].

The aim of this study is to develop a hip prosthesis equipped with a shock-absorbing mechanism that reduces stress by damping sudden and impact loads. Standard prostheses commonly used for the hip joint are generally similar to one another in terms of design and structure. Various types of hip prostheses are available in the healthcare sector, yet these alternatives exhibit comparable shapes and geometries in terms of basic design [12]. To the best of our knowledge, although there are two patents in the literature related to prostheses incorporating springs [13,14], there is no existing study concerning a shock-absorbing hip prosthesis similar to the one proposed in this work. A spring stores a large portion of the energy absorbed during an impact as potential energy. When the applied force is reduced, this stored energy is converted into dynamic motion, creating a rebound effect, which may harm the joint contact surface. In such cases, instead of energy absorption, energy storage and conversion occur. In the newly designed prosthesis, however, a portion of the energy generated by sudden loading is absorbed.

## 2. Materials and Methods

### 2.1. Determination of design criteria

In this study, 316L stainless steel was selected for the design of a spring-damper-based hip prosthesis due to its biocompatibility, high machinability, and cost-effectiveness. 316L stainless steel stands out as a material that should be evaluated for its long-term biological effects. Alternatively, materials with higher biocompatibility, such as titanium and cobalt-chromium alloys, are frequently preferred in prosthetic applications. However, due to the high production and processing costs of these alloys, 316L stainless steel was chosen in this study by considering the balance between performance and cost. Among commercially available shock-absorbing components, standard-type springs and dampers were investigated, and the design process was initiated accordingly. In the literature, a total of 25 human femur bones—12 left and 13 right—have been investigated. The stiffness of the femur bones has been reported as  $k = 757 \text{ N/mm}$  [15]. In this context, the stiffness of the spring to be used in the Type B prosthesis was selected as  $k = 757 \text{ N/mm}$ , matching the bone's stiffness to represent physiological loading. Furthermore, in another study, instrumented hip prostheses were used to measure in-vivo forces during daily life activities involving 10 participants, and the average vertical force was reported as  $F_z = 705.133 \text{ N}$  [16]. Under these loading conditions, a free-body diagram of the prosthesis was constructed (Figure 1). The angle formed between the load vector and the prosthesis neck was calculated as  $\theta = 35.88^\circ$ . Accordingly, the resulting force acting on the neck of the prosthesis was determined to be 571.331 N. To determine the instantaneous velocity value of the damper, a velocity-time curve was generated by taking the gradient of time-displacement curves obtained from the literature [16], as shown in Figure 2.a. Based on data from manufacturers, it was concluded that a damper capable of operating within a reference range of 12–15 mm/s—depending on the applied force and velocity—would be appropriate for effective energy absorption.

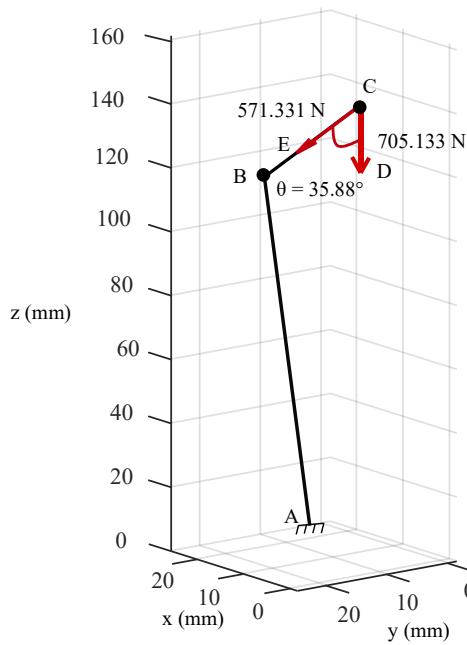


Figure 1. Simple free-body diagram of the prosthesis

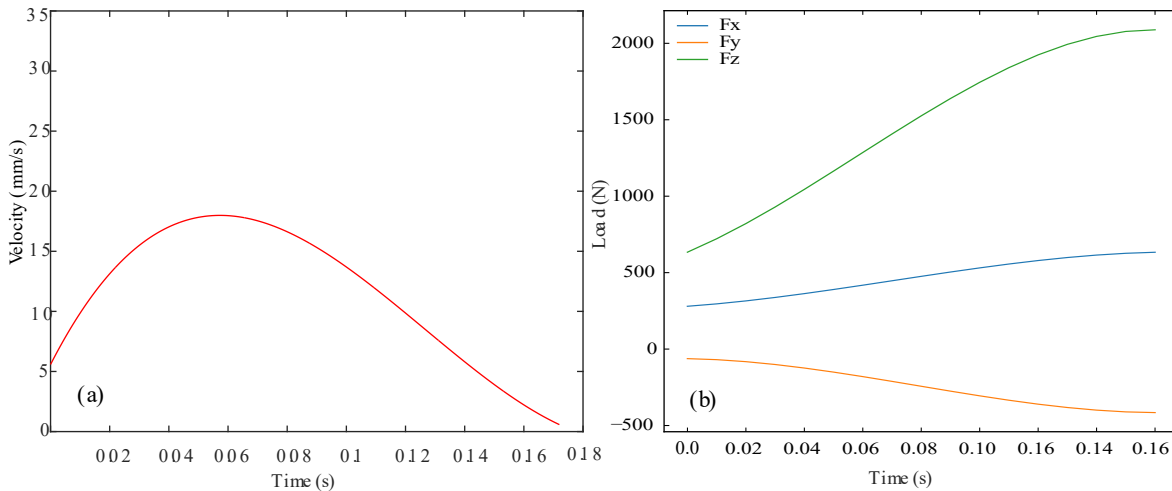


Figure 2. Time-dependent variation of velocity and load at the femoral head during walking. (a) Velocity, (b) Load [16]

Following the determination of the coefficients for the shock absorber and considering the availability of components and manufacturability, three types of prostheses were designed, as illustrated in Figure 3. The standard Type A prosthesis consists of a femoral stem (1) and a femoral head (2). The other types include additional components with the following operating mechanisms. In the Type B prosthesis, when a load is applied to the femoral head (6), the femoral head begins to move over the prosthesis neck (3) due to the polyethylene intermediate ring (5) housed within. Simultaneously, the spring (4), which is integrated with the femoral head, starts to move. In the Type C prosthesis, when a load is applied to the femoral head (11), the femoral head starts to move over the prosthesis neck (7) thanks to the polyethylene intermediate ring (10). At the same time, the damper (9) and spring (8), which are integrated with the femoral head, begin to operate. During the compression phase, the spring (8) compresses to provide elasticity, while the damper (9) compresses to absorption part of the energy.

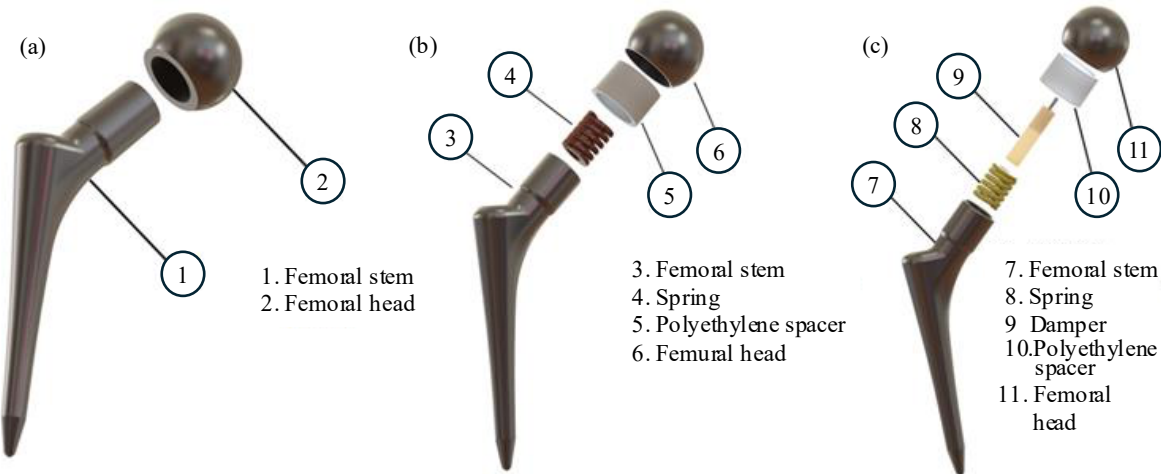


Figure 3. Conventional and proposed prostheses. (a) Type A conventional prosthesis, (b) Type B spring prosthesis, (c) Type C shock-absorbing prosthesis

## 2.2. Finite element analysis

ISO 7206-4 is a standard method that specifies the loading conditions to be applied for evaluating the durability and performance of total hip prostheses in laboratory settings [17]. In this study, all three prosthesis types were analyzed by embedding them into cement according to the lengths and angles specified in the standard. The mesh structure and the number of elements used in the analysis have a significant impact on the results [2,18]. The meshing of the femoral head, cement, and femoral stem for the Type A hip prosthesis was performed using 10-node tetrahedral quadratic (second-order) elements (Figures 4–5). The number of nodes and elements related to the prostheses are presented in Table 1, while the element quality assessment criteria results are detailed in Table 2. The tetrahedral element was preferred due to the complex geometry of the hip prosthesis.

Table 1. Number of nodes and elements of the prostheses

<b>Prosthesis Component Type</b>	<b>Number of Nodes</b>	<b>Number of Elements</b>
<i>A</i>	Femoral head	60838
	Stem	33212
	Cement	72185
<i>B</i>	Femoral head	46523
	Stem	89094
	Polyethylene spacer	40746
<i>C</i>	Femoral head	46523
	Stem	64400
	Polyethylene spacer	40746

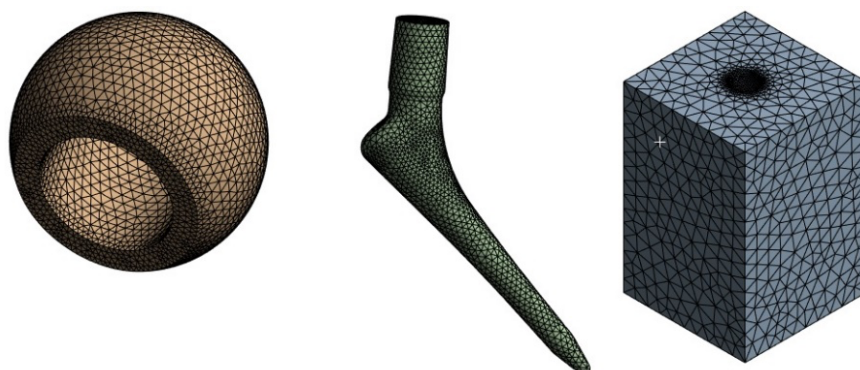


Figure 4. Mesh structure of Type A prosthesis

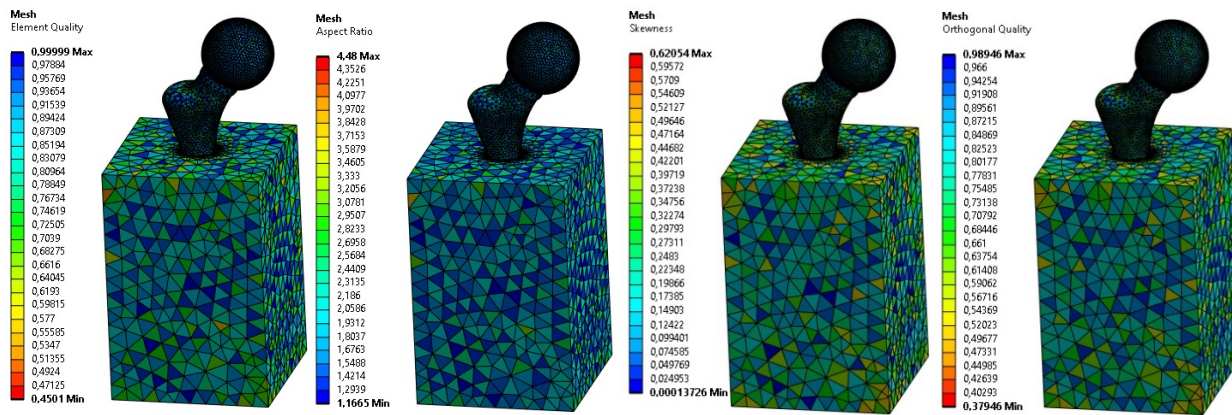


Figure 5. Mesh quality assessment of the Type A prosthesis (Element quality, aspect ratio, skewness, and orthogonal quality)

In the Type B prosthesis, meshing of the femoral head and stem was performed using 10-node tetrahedral quadratic elements, as in the Type A prosthesis (Figures 6–7). Since the cement bodies are identical in all three prosthesis types, remeshing was not required for the cement. However, due to geometric modifications made to the femoral head and stem for spring placement, new meshing was performed for these components. The polyethylene spacer, having a simpler geometry, was meshed using sweep meshing with hexahedral elements. In the Type C prosthesis, since no geometric changes were made to the femoral head, cement, and polyethylene spacer, meshing was only applied to the stem by creating an additional cavity for damper placement (Figure 8).

Table 2. Mesh evaluation criteria of the prostheses

Prosthesis Type	Component	Maximum / Minimum	Element Quality	Aspect Ratio	Skewness	Orthogonal Quality
A	Femoral head	Minimum	0.53935	1.167	0.000	0.465
	Femoral head	Maximum	0.99999	3.642	0.535	0.989
	Femoral stem	Minimum	0.467	1.170	0.000	0.419
	Femoral stem	Maximum	1.000	4.480	0.581	0.989
	Cement	Minimum	0.450	1.174	0.000	0.379
	Cement	Maximum	1.000	4.479	0.621	0.985
B	Femoral head	Minimum	0.53203	1.1634	0.000	0.492
	Femoral head	Maximum	1.000	3.696	0.508	0.988
	Femoral stem	Minimum	0.49124	1.1584	0.000	0.472
	Femoral stem	Maximum	1.000	3.7252	0.52788	0.991
	Polyethylene spacer	Minimum	0.743	1.011	0.011	0.603
	Polyethylene spacer	Maximum	1.000	3.349	0.521	1.000
	Cement	Minimum	0.450	1.174	0.000	0.379
	Cement	Maximum	1.000	4.479	0.621	0.985
C	Femoral head	Minimum	0.53203	1.1634	0.000	0.492
	Femoral head	Maximum	1.000	3.696	0.508	0.988
	Femoral stem	Minimum	0.481	1.166	0.000	0.369
	Femoral stem	Maximum	1.000	4.209	0.631	0.990
	Polyethylene spacer	Minimum	0.743	1.011	0.011	0.603
	Polyethylene spacer	Maximum	1.000	3.349	0.521	1.000
	Cement	Minimum	0.450	1.174	0.000	0.379
	Cement	Maximum	1.000	4.479	0.621	0.985

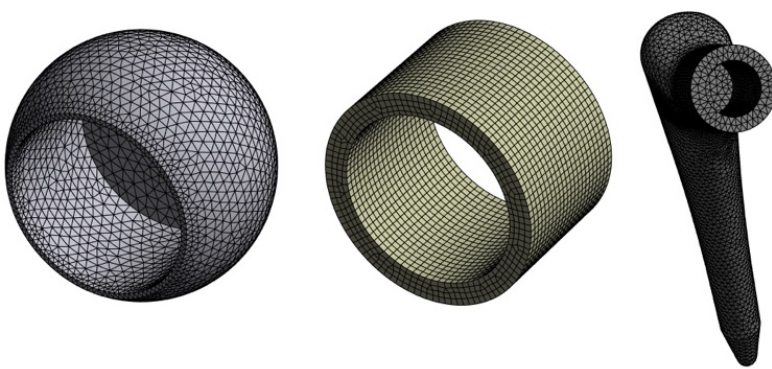


Figure 6. Mesh structure of the Type B prosthesis

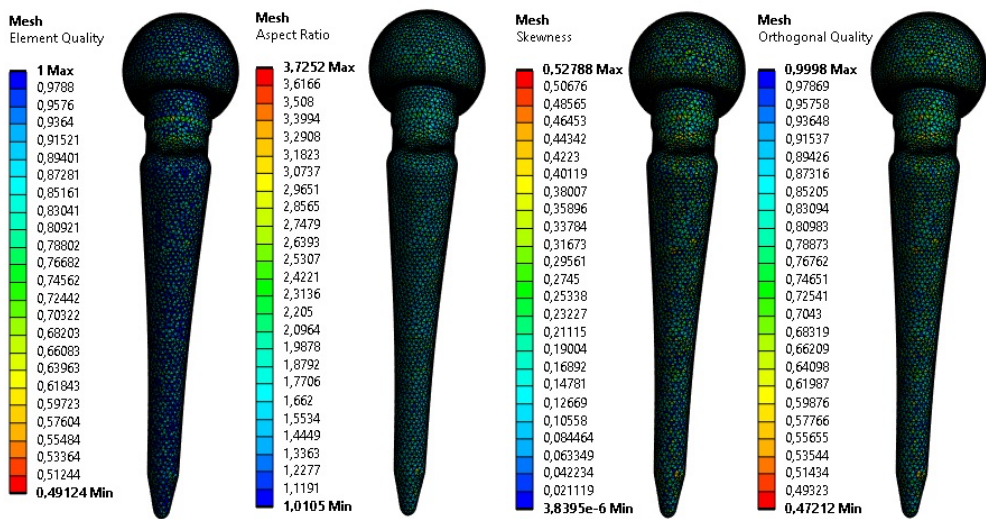


Figure 7. Mesh quality assessment of the Type B prosthesis (Element quality, aspect ratio, skewness, and orthogonal quality)

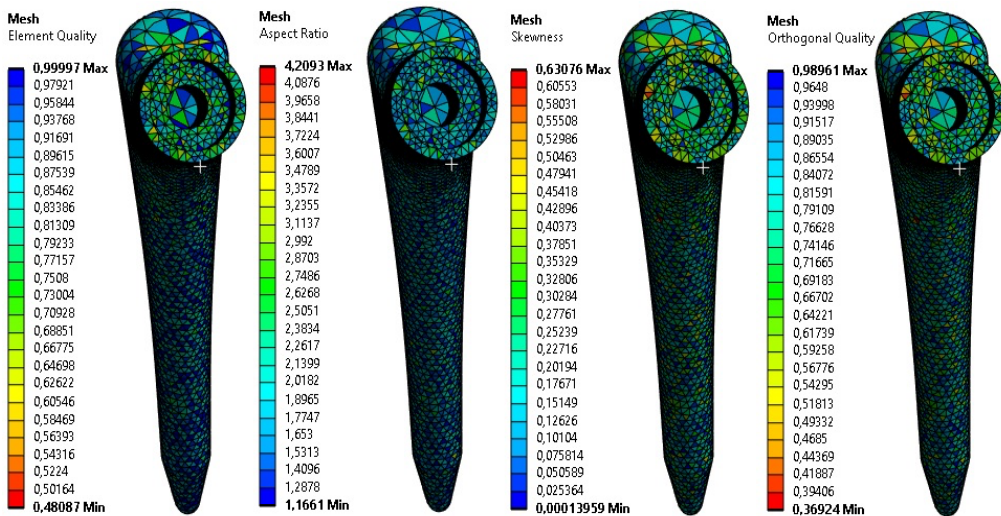


Figure 8. Mesh quality assessment of the Type C prosthesis (Element quality, aspect ratio, skewness, and orthogonal quality)

In all three prosthesis types, loading was applied to cover the surface of the femoral head. The cement component was fixed from five surfaces in total: four lateral 159 face surfaces, and one bottom surface (Figure 9.a). For all three prostheses, loading was applied dynamically using the "Transient" analysis module in the ANSYS environment. The loading conditions used in this study include time-dependent dynamic effects. Therefore, transient analysis was chosen to accurately model the temporal behavior of the system. The loads were applied based on time-dependent data reported in the literature [16], corresponding to forces measured on the femur during normal walking conditions (Figure 2.b).

For all three prosthesis types, the interaction between the portion embedded in the bone cement and the cement itself was defined as bonded (Figure 9.b). In the Type A prosthesis, the contact between the neck and the femoral head was also modeled as bonded (Figure 9.c). In addition to the Type A configuration, the interaction between the polyethylene spacer and the femoral head in Type B and Type C prostheses was likewise defined as bonded, since this connection is designed as a press-fit in the overall design (Figure 9.d). The interaction between the neck region and the polyethylene spacer in Type B and Type C prostheses was defined as a frictional contact (Figure 9.e). The coefficient of friction between the UHMWPE and the metallic surface was assumed to be 0.07 [19].

The spring and damper components of the design were defined using the “Spring” and “Damping” modules available in the ANSYS solver. Based on the calculations presented in the previous sections, the spring stiffness was defined as 757 N/mm, and the damping coefficient was set to 14 Ns/mm in the analysis. Springs and dampers with these coefficients are commonly used in industrial applications.

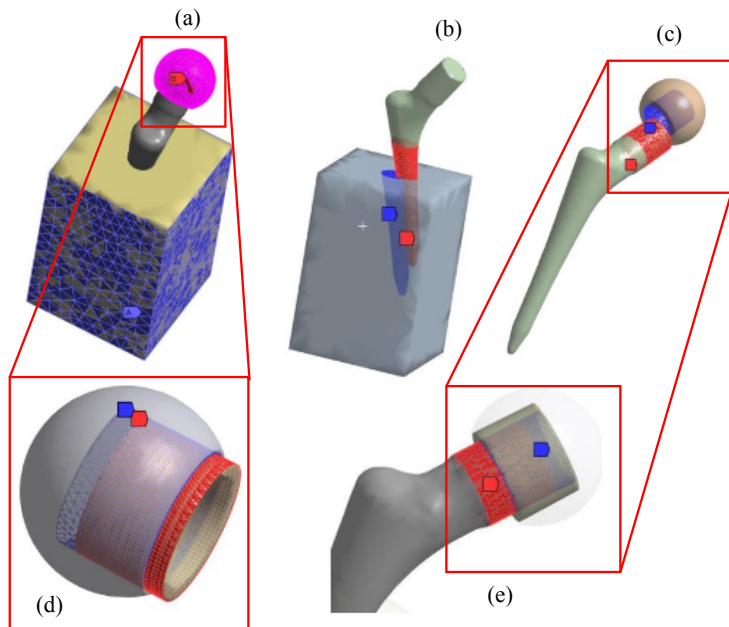


Figure 9. Loading and boundary conditions related to the prostheses. (a) Loading, (b) Interaction between the femoral stem and the cement, (c) Neck-femoral head interaction in the Type A prosthesis, (d) Interaction between the femoral head and the polyethylene spacer in the Type B and Type C prostheses, (e) Interaction between the polyethylene spacer and the prosthesis neck

### 3. Results

The time-dependent maximum stresses, deformations, and strains observed in the prostheses and cement are presented in Figures 10 and 11. For instance, when considering the von Mises stresses in the cement, it was observed that the highest stress occurred in the Type A prosthesis. The maximum stress exerted by the Type A prosthesis on the cement was determined to be 21.919 MPa. For the Type B prosthesis, this value was 14.533 MPa, and for Type C, it was 14.196 MPa. In this context, the Type B prosthesis reduced the stress on the cement by 33.69% compared to the Type A prosthesis. Similarly, the Type C prosthesis achieved a 35.234% reduction compared to Type A, and a 2.318% further reduction compared to Type B. When analyzing the principal strain in the prosthesis stem, the highest value was again observed in the conventional Type A prosthesis.

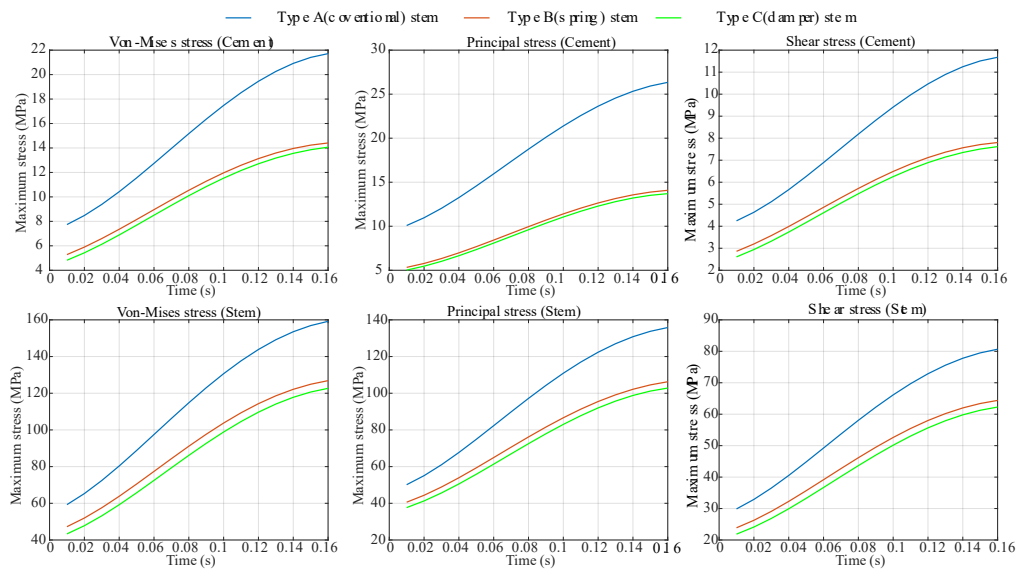


Figure 10. Time-dependent maximum stresses occurring in the prosthesis and cement

The principal strain in the Type A prosthesis stem was calculated as 8.2349E-04, while it was 6.5618E-04 for Type B, and 6.3403E-04 for Type C. Accordingly, the Type B prosthesis achieved a 20.31% reduction in stem strain compared to Type A. The Type C prosthesis showed a 23% reduction compared to Type A, and a 3.375% additional reduction compared to Type B (Figures 10–11). The distributions of von Mises stress, principal stress, and strain in the prostheses are shown in Figures 12, 13, and 14, respectively.

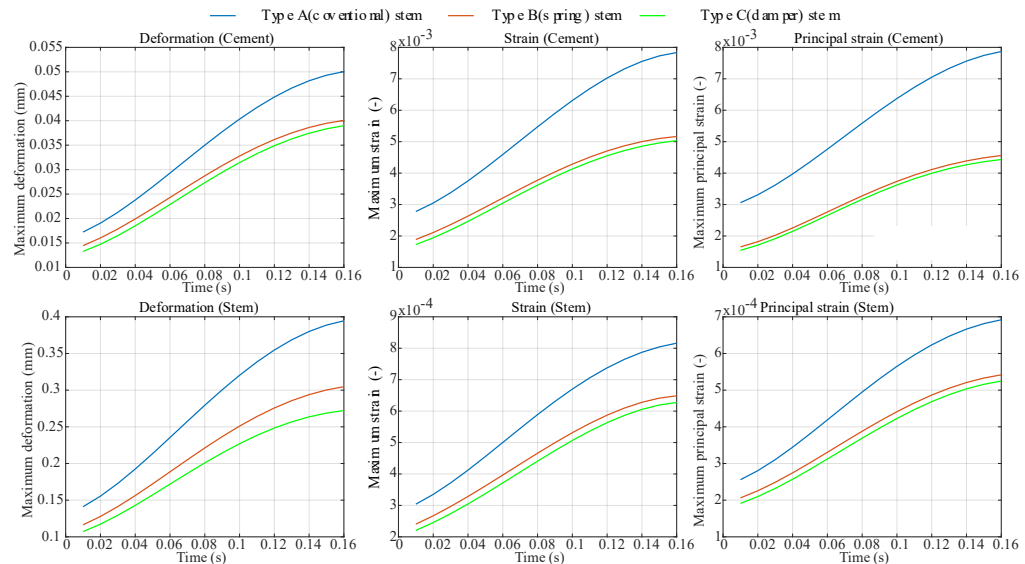


Figure 11. Time-dependent maximum deformation and strain in the prosthesis and cement

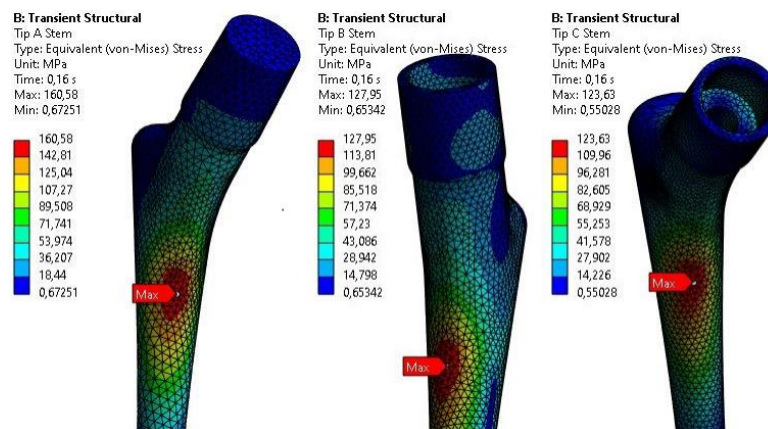


Figure 12. Maximum equivalent (von Mises) stresses in all three prosthesis types

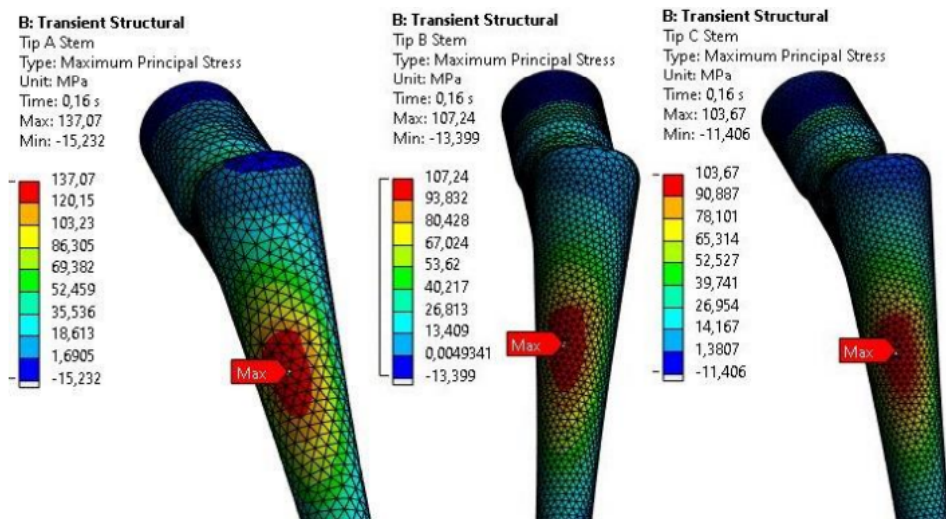


Figure 13. Maximum principal stresses in all three prosthesis types

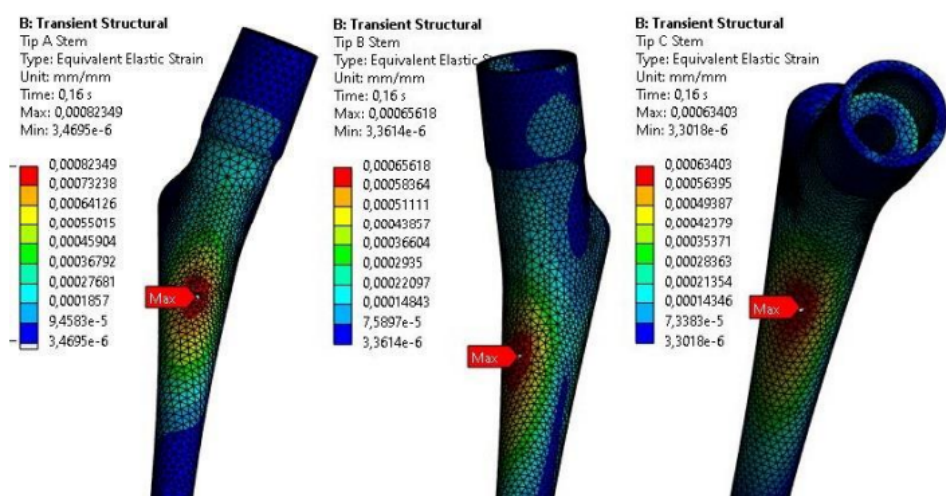


Figure 14. Maximum strain values in all three prosthesis types

#### 4. Discussion and Recommendations

In this study, analyses were performed for both conventional and proposed prostheses by utilizing in vivo forces that occur during daily walking movements in individuals with hip prostheses, as reported in the literature. In the first analysis, the mechanical behavior of the conventional hip prosthesis (Type A) under dynamic loads was investigated. In the second analysis, the performance of a prosthesis with a spring placed between the femoral

head and neck (Type B) under the same loading conditions was evaluated. In the third analysis, the effects of a hip prosthesis incorporating both a spring and a damper (Type C) under the same dynamic loads were assessed. When the effects on the bone cement were assessed, it was observed that the shock-absorbing prosthesis reduced stresses and deformations more effectively compared to the conventional and spring-based prostheses. A review of previous patents revealed that the mechanisms used contained only springs. In such cases, since no energy absorption takes place, all of the energy is stored in the spring. It was found that the use of springs is beneficial in reducing stress. However, during daily use, the hip joint may be subjected to reaction forces. At that moment, the stored potential energy is reflected back into the hip joint after the impact. In the shock-absorbing prosthesis, by contrast, a portion of the energy is absorbed by the damper. During the return motion of the femoral head, this movement occurs much more slowly in the damper-equipped prosthesis compared to the spring response in Type B, allowing a more gradual return to its standard position. The limitations and recommendations within the scope of this study are listed below: Material fatigue, loosening, or loss of viscoelastic properties over time in the spring and damping components may negatively affect the dynamic behavior of the system. A decrease in spring stiffness may lead to insufficient energy storage during impact events, while a reduction in damping coefficient may result in greater transmission of forces and vibrations to the patient. This could reduce comfort during prosthesis use or lead to mechanical problems in the long term. Long-term experimental studies are required to evaluate such effects. It is known that prolonged contact of spring and damping components with living tissue may cause biological reactions such as tissue accumulation or fibrotic capsule formation in these regions. This may restrict the mobility of the system and adversely affect its mechanical performance. Since the primary aim of this study is to evaluate the mechanical efficiency of the system at the engineering level, no specific solution for biological isolation has been developed. However, this issue should be addressed through interdisciplinary studies and is planned to be evaluated more comprehensively in future designs.

The shock absorber model used in this study was created based on the technical specifications of a commercially available product and integrated into the ANSYS environment. The selection of the shock absorber was based on its characteristic being the closest to the damping capacity required to absorb human movement-induced loads. This approach was chosen to model the mechanical response of the system more realistically. However, the potential biological effects of such a damping system in actual implant structures—such as allergic reactions that may occur in the event of leakage—should be considered for long-term use. In this context, the development of biocompatible damping alternatives and the integration of secure isolation systems in future interdisciplinary studies are of critical importance. Therefore, the present study focuses solely on engineering analysis, and the biological effects must be supported by further experimental studies. In our research, due to the lack of spring and damper components compatible with biomedical conditions, industrial-type products were selected. However, these components are not biocompatible. In future studies, the development of springs and dampers suitable for bone physiology and safe for use in the human body would be beneficial. This prosthesis has the potential to contribute to solving loosening problems at the bone–implant interface. However, in addition to numerical analyses, this potential must also be validated through experimental testing.

## Acknowledgment

The authors would like to express their gratitude to Prof. Dr. Fırat Ozan from the Department of Orthopedics and Traumatology, University of Health Sciences, Kayseri City Hospital, for his valuable insights and contributions to this study.

## Conflict of Interest Statement

The authors declare that there is no conflict of interest.

## References

- [1] M. Narin, "Design of a Hip Prosthesis with a Shock Absorber," M.Sc. thesis, Ege University, Graduate School of Natural and Applied Sciences, Izmir, 2024.
- [2] M. Pekedis, A.A. Karaarslan, F. Ozan, M. Tahta, and C. Kayali, "Novel anchor-type proximal femoral nail for the improvement of bone-fixation integrity in treating intertrochanteric fractures: an experimental and computational characterization study," *Computer Methods in Biomechanics and Biomedical Engineering*, pp. 1-17, Jan. 2025. doi:10.1080/10255842.2025.2456985
- [3] M. Pekedis, F. Ozan, and M. Melez, "Location-dependent biomechanical characterization of the human Achilles tendon in diabetic and nondiabetic patients," *ASME Journal of Biomechanical Engineering*, vol. 147, no. 5, pp. 1-18, May 2025. doi:10.1115/1.4068015
- [4] F. Ozan, K.T. Okur, F. Mavi, and M. Pekedis, "Biomechanical and clinical assessment of dissociation in bipolar hip hemiarthroplasty," *Bio-*

*Medical Materials and Engineering*, vol. 36, no. 3, pp. 185-199, Jan. 2025. doi:10.1177/09592989241306688

[5] A. Fontalis, J. A. Epinette, M. Thaler, L. Zagra, V. Khanduja, and F. S. Haddad, "Advances and innovations in total hip arthroplasty," *SICOT-J*, vol. 7, no. 26, pp. 1-10, Apr. 2021. doi:10.1051/sicotj/2021025

[6] A. D. Martino, "Observations on the Present and the Future of Hip Surgery," *Journal of Clinical Medicine*, vol. 12, no. 10, May 2023. doi:10.3390/jcm12103464

[7] K. D. Moore, P.R. Beck, D.W. Petersen, J. M. Cuckler, J. E. Lemons, and A. W. Eberhardt, "Early failure of a cross-linked polyethylene acetabular liner," *The Journal of Bone and Joint Surgery*, vol. 90, no. 11, pp. 2499-2504, Nov. 2008. doi:10.2106/JBJS.G.01304

[8] K. J. Bozic and H. E. Rubash, "The Painful Total Hip Replacement," *Clinical Orthopaedics and Related Research*, vol. 420, pp. 18-25, Mar. 2004. doi:10.1097/00003086-200403000-00004

[9] O. Kayabasi and F. Erzincanli, "Finite element modelling and analysis of a new cemented hip prosthesis," *Advances in Engineering Software*, vol. 37, no. 7, pp. 477-483, July 2006. doi:10.1016/j.advengsoft.2005.09.003

[10] K. Colic, A. Sedmak, A. Grbovic, U. Tatic, S. Sedmak, and B. Djordjevic, "Finite Element Modeling of Hip Implant Static Loading," *Procedia Engineering*, vol. 149, pp. 257-262, 2016. doi:10.1016/j.proeng.2016.06.664

[11] A. Heijink, M. Zobitz, R. Nuyts, B. Morrey, and K. An, "Prosthesis Design and Stress Profile after Hip Resurfacing: A Finite Element Analysis," *Journal of Orthopaedic Surgery*, vol. 16, no. 3, pp. 326-332, Dec. 2008. doi:10.1177/230949900801600312

[12] İ. Mutlu and A. Dizzdar, "Mechanical evaluation of an epiphysis prosthesis as an alternative to conventional total hip prosthesis," *Journal of Polytechnic*, vol. 26, no. 1, pp. 73-79, 2023. doi:10.2339/politeknik.950183

[13] K. Chua, A. K. S. Yew, and N. N. Lo, Hip prosthesis devices, WO Patent 048244, issued 2016.

[14] S. R. Goli and A. Goli, Modular hip implant with shock absorption system, U.S. Patent 0051831A1, issued 2001.

[15] M. Papini, R. Zdero, E. H. Schemitsch, and P. Zalzal, "The biomechanics of human femurs in axial and torsional loading: Comparison of finite element analysis, human cadaveric femurs, and synthetic femurs," *Journal of Biomechanical Engineering*, vol. 129, no. 1, pp. 12-19, 2007. doi:10.1115/1.2401178

[16] G. Bergmann, A. Bender, J. Dymke, G. Duda, and P. Damm, "Standardized Loads Acting in Hip Implants," *PloS One*, vol. 11, no. 5, e0155612, May 2016. doi:10.1371/journal.pone.0155612

[17] International Organization for Standardization, ISO 7206-4: Partial and total hip joint prostheses—Part 4: Determination of endurance properties and performance of stemmed femoral components, ISO Standard 7206-4, 2010

[18] A. Ruggiero, R. D'Amato, and S. Affatato, "Comparison of Meshing Strategies in THR Finite Element Modelling," *Materials*, vol. 12, no. 14, p. 2332, Jul. 2019. doi:10.3390/ma12142332

[19] J. L. Montes-Seguedo, A. L. Garcia-Garcia, J. D. O. Barceinas-Sanchez, et al., "Mapping the friction coefficient of AISI 316L on UHMWPE lubricated with bovine serum to study the effect of loading and entrainment at high values of sliding-to-rolling ratio," *Health Technol.*, vol. 10, pp. 385-390, 2020, doi:10.1007/s12553-019-00355-y

This is an open access article under the CC-BY license



## Gazi Journal of Engineering Sciences

• e-ISSN: 2149-9373 • Founded: 2015 • Period: 3 Issues Per Year • Publisher: Parantez Teknoloji

Search article in the journal

[ABOUT](#)

Gazi Journal of Engineering Sciences (GJES) is an international refereed journal published in the fields of engineering (machinery, construction, industry, computers, etc.) and technology.

The academic publications sent to Gazi Journal of Engineering Sciences are published as open access on the Internet three times a year, after passing through the review of the referees in April, August, and December.

The publication language of Gazi Journal of Engineering Sciences is **English**.

GJES adopts **Budapest Open Access**

137K 606K 70 130

+ Follow

121

All Issues

Contact

[ARCHIVE](#)[Latest Issues](#)

2025 - Volume: 11 Issue: 1

2024 - Volume: 10 Issue: 3

2024 - Volume: 10 Issue: 2

2024 - Volume: 10 Issue: 1

[Early Pub Issues](#)[Special Issues](#)[EXPLORE](#)

Submit a Manuscript

Send Reviewer Request

Aim & Scope

Author Guidelines

Ethical Principles and Publication Policy

Price Policy

Journal Boards

Statistics

CURRENT ISSUE ARTICLES IN PRESS

grid list

Research Article

2-D Geometric Accuracy Investigation of Vat-Photopolymerisation Printed Yttrium Stabilised Zirconia Ceramics

Fatih Tarak \* Basar Ozkan Ehsan Sabet

Application Date: Dec 3, 2024, In Press Date: May 16, 2025

Research Article

Gerçek Zamanlı Mermi Kovarı Kalite Kontrol Sistemi Tasarımı

Kerem Albayrak \* Adnan Akkurt

Application Date: Aug 24, 2024, In Press Date: May 24, 2025

Review

A Comprehensive Review of Wrist-Hand Orthoses: Biomechanics and Additive Manufacturing

Ahmet Gökhan Acar Harun Gökcé \* Serap Alsancak

Application Date: Apr 29, 2025, In Press Date: Jun 4, 2025

Research Article

Hip Prosthesis Design with a Shock Absorber

Mert Narin Mahmut Pekedis \*

Application Date: Mar 7, 2025, In Press Date: Jun 4, 2025

Research Article

Effects of Thermal Spray Coatings on Surface Protection and Mechanical Performance of AlSi10Mg Alloy Produced by Additive Manufacturing

Abdülcelil Bayar Gözde Altuntaş \*

Application Date: Mar 19, 2025, In Press Date: Jul 9, 2025

Research Article

Proposal for a UAV-Integrated Manipulator-Based System for Capturing Animals with Anesthesia: Simulation and Experimental-Based Validation

Nihat Çabuk \*

Application Date: Nov 7, 2024, In Press Date: Jul 9, 2025

RSS

GJES is indexed and archived by:



CiteFactor  
Academic Scientific Journals

INDEX COPERNICUS  
INTERNATIONAL



## **Yumuşak Dokunun Biyomekanik Karakterizasyonu için iki Eksenli Çekme-Basma Test Cihazı**

## **The Biaxial Tension-Compression Test Device for the Biomechanical Characterization of Soft Tissue**

**Schirin Schirinova<sup>1</sup>, Saran Sapmaz<sup>1</sup> , Devrim Tümer<sup>1</sup>, Coşhun Harmanşah<sup>2</sup>, Mahmut Pekedis<sup>1\*</sup>**

<sup>1</sup>Ege Üniversitesi Mühendislik Fakültesi Makina Mühendisliği, İzmir, TÜRKİYE

<sup>2</sup>Ege Üniversitesi, Ege Meslek Yüksekokulu, Bilgisayar Programcılığı Programı, İzmir, TÜRKİYE

*Sorumlu Yazar / Corresponding Author \*:* mahmut.pekedis@ege.edu.tr

### **Özet**

Anizotropik malzemelerin iki eksende mekanik davranışlarını tespit etmek için mevcut olan endüstriyel çift eksenli makineler oldukça maliyetlidir. Bu çalışmada, evrensel çekme-basma cihazlarıyla uyumlu çalışabilecek basit, ekonomik ve pratik iki eksenli çekme-basma cihazı geliştirilmiştir. Cihaz anizotropik ve doğrusal olmayan davranış sergileyen Aşıl tendonu üzerinde test edilmiştir. Cihaz yük taşıyıcı elemanlar, hareketi sağlayan doğrusal ray ve arabalar, numune tutucu çeneler, birim şekil değiştirme rozetleri ve veri alım ünitesinden oluşmaktadır. Öncelikle kasaptan temin edilen dana Aşıl tendonlarından, bir yönü fibere paralel, diğer yönü ise fibere dik doğrultuda olacak şekilde "arti (+)" şeklinde örnekler çıkarılmış ve örnekler geliştirilen cihazla test edilmiştir. Elde edilen ölçütler filtrelemeye tabi tutulmuştur. Daha sonra bu ölçütler Ogden malzeme modelinde değerlendirilmiş ve eğri uydurma teknikleriyle numuneye ilişkin parametreler belirlenmiştir. Bu çalışmada geliştirilen portatif ve ekonomik cihaz ile beraberinde uygulanan metodolojik yaklaşım, anizotropik yumuşak doku biyomekaniği alanına önemli katkılar sağlayabilecektir.

**Anahtar Kelimeler:** İki eksenli test, Ogden modeli, biyomekanik karakterizasyon, yumuşak dokular

### **Abstract**

The current biaxial industrial devices used to characterize the mechanical behavior of anisotropic materials in two axes are quite costly. In this study, a simple, economical and practical biaxial tension-compression device that is compatible with universal tensile test machines is developed. It is implemented on Achilles tendon which shows a nonlinear anisotropic mechanical response. The device consists of structural components that transfer loads, linear rails and cars that allow motion, grippers that fixate the specimen, strain gauges and a data acquisition unit. Initially, specimens, obtained from a slaughter shop, were harvested, re-sectioned with a "cross (+)" sign, in which one of the directions is aligned parallel to the fiber directions and the other is directed perpendicular to the fibers. The specimens were tested with the developed device. The collected measurements were filtered. Then, they were evaluated in the Ogden material model to identify the specimen-specific material parameters using curve fitting techniques. The portable and economical device developed in this study and the methodological approach used have the potential to make significant contributions to the field of anisotropic soft tissue biomechanics.

**Keywords:** Biaxial testing, Ogden model, biomechanical characterization, soft tissues

### **EXTENDED ABSTRACT**

#### **Introduction**

The biaxial testing of soft tissues is of critical importance for the accurate determination of their mechanical properties [1]. Due to the fibrous structures and tissue characteristics, elastic and plastic deformations occur in soft tissues. The biomechanical characterization of such materials relies on data obtained through correct testing methods.

Biaxial testing machines are generally more expensive than uniaxial machines because their structures are more complex, which requires additional actuators and components. Therefore,

various devices that create a biaxial loading condition in uniaxial testing machines are available in the literature.

A comprehensive review of different devices for biaxial loading provides detailed information on devices with actuators in each loading direction and devices designed for use in uniaxial machines [2]. Other approaches for biaxial loading [3], such as planar and 3D mechanisms [4], are also discussed in the literature.

The aim of this study is to design and manufacture a mechanical device that can be integrated into a uniaxial testing machine and allows biaxial testing of soft tissues. The device enables the

application of biaxial tests with simple manipulations. The device is designed for biaxial loading, proper alignment and the creation of an appropriate loading condition for soft tissues must be ensured. The correct alignment of the device is critical for obtaining representative results. Our hypothesis is that the designed device successfully provides the required standard loading conditions for biaxial testing of soft tissue samples [5-8].

## Materials and Methods

The mechanism's design was carried out in accordance with the dimensions of the universal tensile electromechanical testing machine. The design parameters assure that the device's width must not exceed 40 cm and its height must not exceed 50 cm. To optimize portability and reduce weight, the mechanism was constructed using aluminum components. It consists of various components that have been designed to match the dimensions of the electromechanical testing machine. The testing machine has the capacity to generate cyclic loads and apply a force of up to 100 kN along the vertical axis.

The test setup for the proposed mechanism consists of specially developed clamps (Figure 1). The experiments were performed at a speed of 20 mm/min, and the force and displacement values obtained during the tests were recorded similar to previous studies [9, 10]. HGH 15 CA BGR-type linear guides were used to ensure smooth and precise motion along both axes.

The force on each axis was determined using strain gauges. Prior to testing, the samples were resectioned into a plus ('+') shape (Figure 2). Once the samples were prepared, they were

moistened with isotonic water to preserve their viscoelastic properties [3, 4]. The measurements were obtained from the gripper's kinematics and the strain gauge attached to the gripper using LabVIEW software (Figure 3-4). The experimental data were fitted to Ogden model using Python. The root mean square error (RMSE) was used as objective function during optimization of model parameters.

## Results and Discussion

Using the biaxial testing device, tests were implemented on tendon samples. The data showed that stresses were generally lower in the transverse direction than in the fiber direction. Nonlinear curve fitting using the Ogden model yielded low RMSE values for both directions, affirming the model's effectiveness in representing tendon mechanics under biaxial loading conditions (Figure 5). This outcome underlines the importance of multi-directional testing for obtaining comprehensive mechanical profiles of soft tissues.

## Conclusion

The newly developed biaxial testing device, and the measurements coupled with the Ogden model, offers a reliable approach for characterizing the mechanical properties of soft tissues. This research advances the understanding of soft tissue mechanics and lays a foundation for further exploration of other hyperelastic models. Future studies should expand testing conditions and sample diversity to assess the robustness of this model across various tissue types and age groups. Additionally, 3D stress analyses and numerical simulations could further enrich our biomechanical insights, contributing valuable knowledge for both clinical and theoretical applications.

## 1. Giriş

Yumuşak dokuların çift eksenli olarak test edilmesi, mekanik özelliklerinin doğru bir şekilde belirlenebilmesi için önemlidir [1]. Yumuşak dokularda lifli yapıları ve doku özellikleri nedeniyle elastik ve plastik deformasyonlar meydana gelir. Bu tür malzemelerin biyomekanik karakterizasyonu, doğru test yöntemleriyle elde edilen ölçümlere dayanır.

Çift eksenli test makineleri, genellikle tek eksenli makinelerden daha maliyetlidir. Yapıları daha karmaşık olduğu için daha fazla aktuatör ve ek bileşen gerektirir [2]. Bu nedenle, tek eksenli test makinelerinde iki eksen yükleme durumunu üretmeye yönelik çeşitli cihazlar literatürde sunulmuştur [2, 11]. Bununla beraber, her yükleme ekseninde aktuatör barındıran cihazlar ve tek eksenli makinelerle beraber kullanılmak için geliştirilmiş bazı aparatlar incelenmiştir [2, 11, 12]. Ayrıca, düzlem içi [13] ve farklı yüklemeleri test edebilen bazı mekanizmalar [4] literatürde yer almaktadır.

Bu çalışmanın amacı, yumuşak dokulara özel ve evrensel tek eksenli test makinelerine entegre edilebilen, aynı zamanda yumuşak dokuların iki eksenli testlerinin gerçekleştirilebildiği basit bir cihaz tasarlamak, üretmek ve bu cihazın yumuşak dokular üzerindeki etkinliğini değerlendirmektir. Cihazın en önemli özelliği, evrensel çekme-basma makinesinin oluşturduğu tek eksenli dikey yükü, yatay düzlemede iki eksene aktarılabilmesidir. Bu sayede, şekil değişimi yüksek olan damar, deri ve kas gibi izotropik olmayan yumuşak dokular bu cihaz

kullanılarak test edilebilmektedir. Literatürde, tek eksenli test makinelerine entegre edilebilen iki eksenli test cihazları tasarlanmış ve genellikle kompozit malzemeler üzerinde testler gerçekleştirilmiştir [20]. Ayrıca, yumuşak doku karakterizasyonu amacıyla iki eksenli test cihazı geliştirilmiş ve bu cihaz yumuşak dokular üzerinde test edilmiştir [21]. Mevcut çift eksenli cihazlar genellikle yüksek maliyetli ve karmaşık yapılara sahipken, bu çalışmada önerilen cihaz; düşük maliyet, taşınlabilirlik ve evrensel test makineleriyle kolay entegrasyon gibi avantajlar sunmaktadır.

## 2. Materyal ve Metot

Önerilen iki eksenli test cihazının, literatürde yumuşak dokuların biyomekanik karakterizasyonu üzerine gerçekleştirilen çalışmalarla yer alan standart yükleme koşullarını başarıyla sağlaması gereklidir [5]. Bu kapsamda, cihaza ilişkin mekanizmanın, evrensel test makinelerinin boyutlarına uygun olacak şekilde tasarlanması gereklidir [8]. Tasarım parametreleri cihaz genişliği 40 cm ve yüksekliği 50 cm'i aşmayacak şekilde seçilmiştir. Bu kısıtlamalar hem biyomekanik test cihazlarının taşınlabilirliğini hem de kullanım kolaylığı açısından çok önemlidir [1, 6]. Bununla birlikte cihaz yumuşak dokulara özel tasarlandığı için numuneler düşük yüklerle maruz kalır ve bu yüzden cihaz alüminyumdan üretilmiştir (Şekil 1). Bu hem hafiflik hem de taşınlabilirlik açısından avantaj sağlar [7].

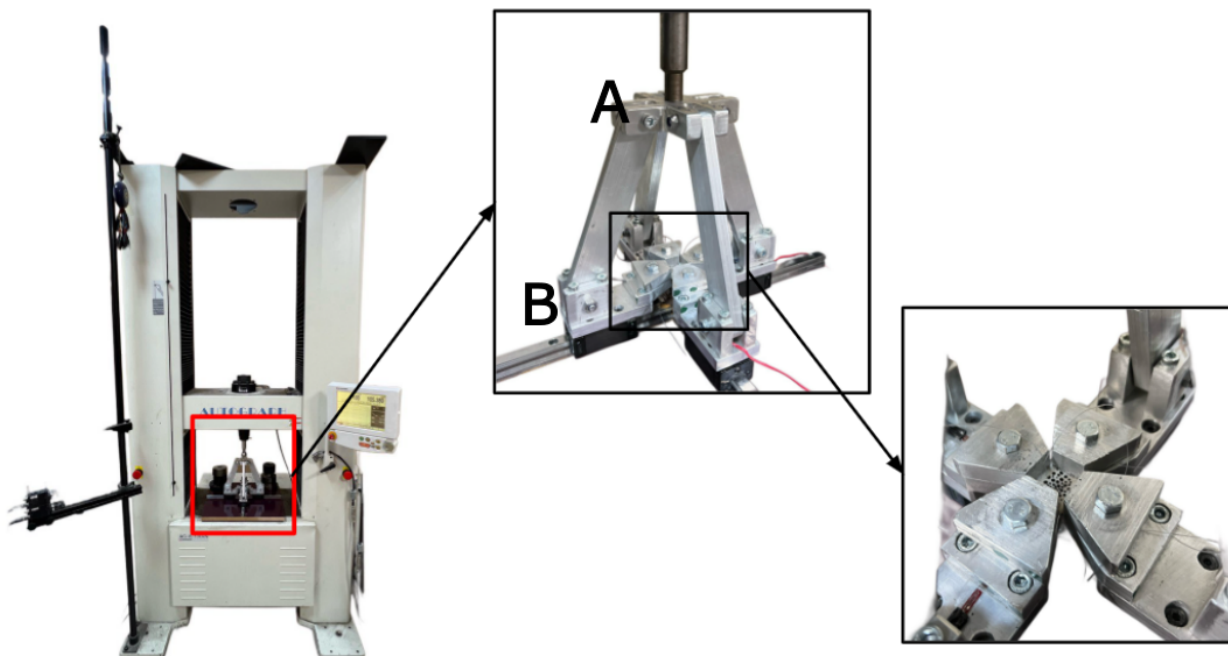
Cihaz genel olarak yük taşıyıcı elemanlar, hareketi sağlayan doğrusal ray ve arabalar, numune tutucu çeneler, birim şekil değiştirme rozetleri ve veri alım ünitesinden oluşmaktadır. İki

eksende düzgün ve hassas hareketi sağlamak için HGH 15 CA BGR tipi doğrusal arabalar kullanılmıştır. Bu tür doğrusal arabaların yüksek hassasiyet ve dayanıklılık avantajları biyomekanik testlerde yaygın olarak kullanılmaktadır [2]. Test sürecinde numune üzerinde olacak tepki kuvveti yatay olarak konumlandırılan iki kuvvet sensörü ile belirlenebilir. Ancak bu kuvvet sensörleri maliyetlidir. Bunların yerine yatay olarak konumlandırılmış çenelerin yer aldığı elemanlarda tek eksenli birim şekil değiştirme sensörleri yerleştirilmiş ve temel doğrusal şekil değiştirme-gerilme bağıntılarıyla kuvvetin değerini hesaplanmıştır. Bunlara ilişkin detaylar 2.4. bölümünde açıklanmıştır.

Tüm numuneler, artı ('+') biçiminde çıkarılmıştır (Şekil 2). Test öncesinde numunelerin viskoelastik özelliklerinin korunmasını sağlamak için izotonik su ile nemlendirme işlemi yapılmıştır. Bu yöntem, yumuşak doku numunelerinin fizyolojik özelliklerini korumada etkili bir yöntem olarak bilinmektedir [3, 10, 14]. Deneyler, 20 mm/dk (dikey yük) hızında gerçekleştirilmiş ve test sırasında belirlenen iki yatay düzlemdeki kuvvet ile yer değiştirme değerleri Ogden modelinde değerlendirilmiş ve eğri uydurma tekniğiyle modele ilişkin parametreler tespit edilmiştir. Ogden modelinin yumuşak dokuların mekanik özelliklerinin belirlenmesinde yaygın olarak kullanılan hiperelastik bir bünye modeli olduğu bilinmektedir [6, 14]. Model parametrelerinin doğruluğunu artırmak için amaç fonksiyonu olarak kök ortalama kare hatası (root mean square error "RMSE") tekniği kullanılmıştır [13]. Çalışmanın gerçekleştirilemesi aşamasında uygulanan teknik yöntem ve yaklaşımlar ayrıntılı olarak ilerleyen başlıklarda sunulmuştur.

Geliştirilen deney seti, mevcut evrensel bir elektromekanik çekme-basma cihazına entegre edilmek üzere tasarlanmıştır [16]. Bu yönyle sistem, standart iki eksenli testler için pratik ve ekonomik bir çözüm sunmaktadır. Evrensel çekme-basma cihazındaki kuvvet sensörü, dikey eksende 100 kN'a kadar yük uygulayabilme kapasitesine sahiptir [17-18]. Bu çalışmada, çift eksenli yükleme sağlamak amacıyla, evrensel makinanın ürettiği dikey eksendeki yükü yatay ve dikey eksenlere dağıtan basit bir mekanizma geliştirilmiştir. Bu mekanizma, yük taşıyıcı elemanlardan oluşmakta ve numuneye aynı anda iki farklı eksende çekme veya basma kuvveti uygulayarak test yapılmasını sağlamaktadır [1]. Her eksende zamana bağlı olarak oluşan yer değiştirme (Bölüm 2.4'te verilen kinematik denklemler ve rıjt cisim kabulu doğrultusunda) evrensel makina aracılığıyla kontrol edilebilse de, tendonlardaki anizotropik davranış nedeniyle her iki eksende oluşan yükün bağımsız olarak kontrol edilmesi mümkün olmamaktadır. Kinematik olarak her bir eleman hem dönme hem de öteleme hareketi yapmaktadır. Elemanların alt uçlarına pimli bağlantılarla monte edilen doğrusal arabalar, sürtünmeden kaynaklı tepki kuvvetini azaltarak deney setinin yatay deformasyonu her iki eksende de eşit olarak dağıtmamasına olanak tanır [3].

Numunelerin güvenli bir şekilde sabitlenmesi için mekanizma üzerine monte edilmiş özel sabitleme çeneleri tasarlanmıştır (Şekil 1). Bu aparatlar civatalarla cihaza bağlandığından dolayı bunlar değiştirilerek farklı konfigürasyonda çene takılabilir. Veri toplama sürecinde evrensel makinanın dikey yer değiştirmesi ile çenelerin bağlılığı elemanlarda yer alan birim şekil değiştirme rozetlerinin verileri kullanılmıştır. Bu rozetler, yükleme esnasında eksenel deformasyonun hassas bir şekilde ölçülmesini



**Şekil 1.** İki eksenli çekme-basma deney seti.

**Figure 1.** Biaxial tension-compression test setup.

## 2.1. İki Eksenli Çekme-Basma Deney Seti Kurulumu

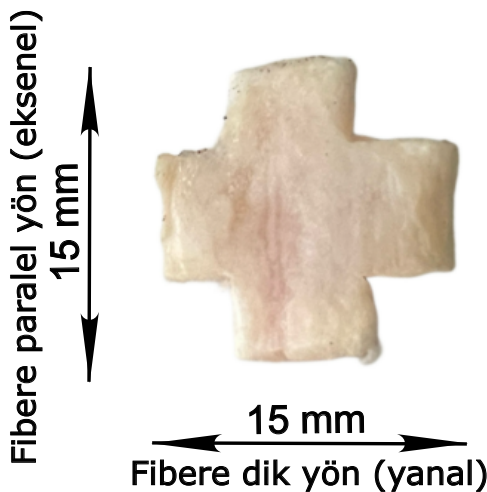
sağlar [15]. Bu çalışmada kullandığımız birim şekil değiştirme rozetinin gauge direnci 120 ohms ve gauge uzunluğu ise 2.12 mm'dır.

Yüksek hassasiyetli HGH 15 CA BGR tipi arabalar hem statik hem de dinamik yük kapasitesiyle mekanizmanın dayanıklılığını arttırır. Bu arabalar, kompakt ve hafif tasarımları sayesinde

yüksek hassasiyetli hareket sağlamaktadır. Aynı şekilde yüksek kütle taşıma kapasitesine sahiptir (dinamik 1138 kg, statik 1697 kg'a kadar).

## 2.2. Numune Hazırlama

Test öncesinde, numuneler artı biçiminde kesilip kullanılan tendon örnekleri ( $n = 3$ ), kasaptan temin edilmiş ve örnekler teste kadar derin dondurucuda  $-20^{\circ}\text{C}$  sıcaklıkta bekletilmiştir. Tendon örneklerinin boyutları, mümkün olduğunda  $15 \text{ mm} \times 15 \text{ mm}'\text{yi}$  geçmeyecek şekilde çıkarılmıştır. Örnekler çözüldükten sonra, tendonların viskoelastik özelliklerinin korunması amacıyla izotonik sıvı solüsyonu ile nemlendirilmiştir. Numuneler test edildeden önce, her bir tendon örneği fibere dik ve paralel olarak cihaza yerleştirilmiş ve iki eksenli çekme testine tabi tutulmuştur. Fiber doğrultusuna paralel olan yön eksenel eksen, dik olan yön ise yanal eksen olarak tanımlanmıştır. Bu yönler, tendonların mekanik özelliklerini etkileyen önemli faktörlere dir. Fiberin paralel (eksenel) yönü, tendonu oluşturan kolajen liflerinin yönünü, fiberin dik (yanal) yönü ise bunların çevresindeki ekstraselüler matriksin yapısını ifade eder. Bu doğrultuda, fiber yönü testin doğruluğunu etkileyebilecek kritik bir parametre olarak dikkate alınmıştır. Fiber yönüne paralel ve dikey olarak yerleştirilen örnekler test sırasında daha gerçekçi ve tutarlı sonuçlar elde edilmesini sağlar [5].



**Şekil 2.** "Artı" şeklindeki tipik bir tendon numunesi

**Figure 2.** A typical tendon specimen with a 'cross' form

## 2.3. İki Eksen Çekme Durumu İçin Hiperelastik Ogden modeli

Ogden modeli, doğrusal olmayan ve yüksek değişimi barındıran kauçuk ve yumuşak doku gibi malzemelerinin mekanik davranışlarını matematiksel olarak tarif eden bir çeşit hiperelastik bünye modelidir. Bu çalışmada her numuneye ilişkin ölçümler Ogden malzeme modelinde değerlendirilmiş ve eğri uydurma teknikleriyle numuneye ilişkin parametreler belirlenmiştir. Doğrusal olmayan eğri uydurma sürecinde Python SciPy kütüphanesi kullanılmıştır. Ogden modelinde birim şekil değiştirme enerji yoğunluğu fonksiyonu şu şekilde ifade edilir [19]:

$$W = \sum_{i=1}^n \frac{2\mu_i}{\alpha_i^2} [(\lambda_1^{\alpha_i} + \lambda_2^{\alpha_i} + (\lambda_1\lambda_2)^{-\alpha_i} - 3)] \quad (1)$$

Burada:  $\lambda_1$  ve  $\lambda_2$  uzamayı (stretch  $\varepsilon+1$ ) gösterir.  $\mu_i$  ve  $\alpha_i$  Ogden modeline ilişkin  $i$ 'nci mertebedeki parametrelerdir. Burada  $n=3$  kabul edilmiştir. Parantez içerisinde verilen  $\varepsilon$ , birim şekil değişimini, 1 ve 2 indisi ise sırasıyla fibere paralel ve fibere dik olan yönleri gösterir. Birim şekil değiştirme enerji fonksiyonun her yöndeki uzamaya bağlı türevlerinin alınmasıyla gerilme-uzama (stress-stretch) ilişkisi bulunur.

## 2.4. Kinematik Analiz

Şekil 3, Şekil 1'deki deney düzeneğinde yer alan taşıyıcı bir elemanın hareketini analiz edebilmek amacıyla oluşturulan basitleştirilmiş geometrik modeli göstermektedir. Burada  $V_A$  evrensel makinannın dikey basma hızını göstermektedir ve test süresince sabittir. A noktasının konumu  $t$  süresine bağlı

$$y_A(t) = y_{A_0} - V_A t \quad (2)$$

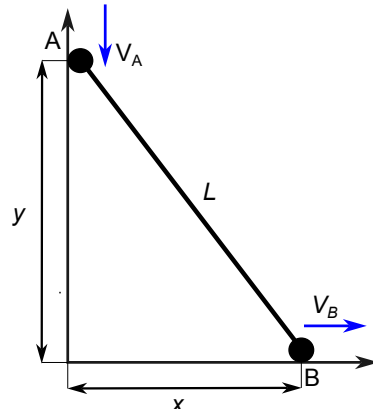
olar. Burada  $y_{A_0}$ , A noktasının başlangıç konumunu gösterir. Geometrik bağıntıdan aşağıdaki denklem yazılabilir.

$$L = \sqrt{y_A^2 + x_B^2} \quad (3)$$

Denklem düzenlenirse B noktasının zamana bağlı konumu aşağıdaki gibi yazılabilir.

$$x_B(t) = \sqrt{L^2 - y_A(t)^2} \quad (4)$$

B noktasının hareket miktarı  $x_B(t) - x_{B_0}$  olup,  $x_{B_0}$  B noktasının başlangıç konumunu gösterir.  $x_B(t) - x_{B_0}$  değeri aynı zamanda yatay olarak konumlandırılan çenelerdeki yer değiştirmeyi ( $d$ ) temsil eder.  $L$  sabit olup  $x_{B_0}$  ise her test öncesi ölçülmüştür.



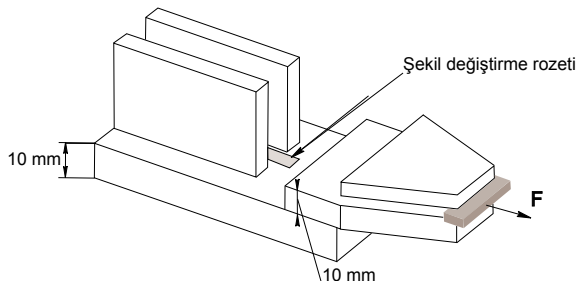
**Şekil 3.** İki eksenli test cihazındaki çenenin kinematiği

**Figure 3.** Gripper kinematics for the biaxial testing device

## 2.5. Gerilme ve Şekil Değiştirme Analizi

Şekil 4'te, çeneye aynı eksende yerleştirilmiş tek eksenli bir birim şekil değiştirme rozeti gösterilmiştir. Rozetten elde edilen veriler, 24 bitlik NI 9237 modülü kullanılarak 1612,9 Hz örneklemeye hızında toplanmış ve LabVIEW yazılımı ile işlenmiştir. Rozette oluşan deformasyon, hem  $F$  kuvveti hem de  $M$  momentinin oluşturduğu eksenel gerilmeden kaynaklanmaktadır. Bu durumda eksantrik bir yükleme söz konusu olup aşağıdaki denklem yazılabilir.

$$\sigma = \frac{F}{ch} + \frac{M \cdot (h/2)}{I} \quad (5)$$



**Şekil 4.** Birim şekil değiştirme rozetinin (strain gauge) yerleştirildiği bölge.

**Figure 4.** The region where the strain gauge is attached.

Denklem 5'te,  $I = \frac{c h^3}{12}$  olup atalet momentini,  $c$  rozetin iliştirildiği bloğun genişliğini ( $c=40$  mm),  $h$  kalınlığını ( $h=10$  mm),  $t$  ise numune kalınlığını ( $t=3$  mm) gösterir. Moment ise  $M = F(h + t/2)$  şeklinde hesaplanır. Gerilme ( $\sigma$ ) ile şekil değiştirme ( $\varepsilon$ ) arasındaki ilişki Hooke yasasına göre aşağıdaki gibidir.

$$\sigma = E \varepsilon \quad (6)$$

Damar, kas, tendon ve ligament gibi yumuşak dokuların anizotropik özelliklerini nedeniyle, bu dokuların mekanik özelliklerinin doğru şekilde belirlenebilmesi için çift eksenli testlerin uygulanması önem taşımaktadır [22-25]. Bu çalışma kapsamında, yumuşak doku mekanik karakterizasyonu amacıyla çift eksenli bir test cihazı tasarlanmış ve üretilmiştir. Geliştirilen cihazın etkinliği, dana Aşıl tendonları üzerinde test edilmiştir. Aşıl tendon örneklerinin çift eksenli test sonuçları, fiber yönüne paralel ve fibere dik doğrultulardaki mekanik davranışlar açısından değerlendirilmiştir. Elde edilen sonuçlar, fiber yönüne paralel doğrultuda daha yüksek gerilme değerleri gösterirken, fibere dik yöndeki gerilmelerin belirgin şekilde düşük olduğunu ortaya koymuştur. Bu bulgular, literatürdeki benzer çalışmalarla uyumludur. Daha önceki araştırmalarda da yumuşak dokuların lifli yapısı nedeniyle anizotropik davranış sergilediği ve fiber yönüne paralel uygulanan yüklemelerde daha yüksek gerilme dayanımı gözleendiği bildirilmiştir [1, 6]. Bizim bulgularımız da bu literatür sonuçlarını desteklemektedir. Ayrıca, önceki çalışmalarla paralel olarak, başlangıçta fiberlerin eksenel doğrultusunda hasar oluştuğu, ardından fibere dik (yanal) doğrultudaki hasarların ortaya çıktığı gözlemlenmiştir [6]. Bunun yanında, eksenel yönde oluşan maksimum gerilmenin yanal yöndeki gerilmeye oranının daha önce sunulan çalışmalarla

**Tablo 1.** Ogden modeliyle belirlenen parametreler. Table 1. Parameters identified using Ogden model

Numune	n	Fibere paralel yön (eksenel)			Fibere dik yön (yanal)		
		$m$ (MPa)	$\alpha$ (-)	RMSE (MPa)	$m$ (MPa)	$\alpha$ (-)	RMSE (MPa)
1	1	19.99	0.112		5.165E-02	9.99	
	2	0.68	6.82	0.08	1.922E+01	0.1	0.098
	3	19.99	0.116		3.5526E-06	0.14	
2	1	0.041	9.99		4.908E+00	0.1	
	2	1.517	0.10	0.037	9.550E-03	10.0	0.136
	3	19.99	0.1		1.186E-04	0.10	
3	1	19.97	0.1		6.023E-04	0.10	
	2	0.058	9.9	0.027	3.123E-02	9.99	0.136
	3	1.12	0.10		1.170E+01	0.1	

n: Ogden modelinde kullanılan mertebe gösterir, RMSE ise kök ortalama kare hatasıdır.

Üstte verilen denklemler beraber düzenlenerek eksenel kuvvet aşağıdaki gibi belirlenebilir.

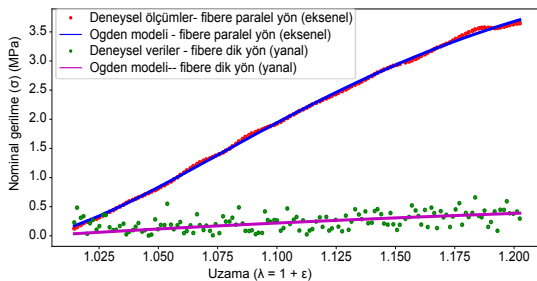
$$F = \frac{E \cdot \varepsilon \cdot c \cdot h}{7 + \frac{3t}{h}} \quad (7)$$

Rozetlerin monte edildiği yük taşıyıcı eleman, elastisite modülü ( $E$ ) 70 GPa olan alüminyumdan üretilmiştir.  $\varepsilon$  rozetlerden okunan şekil değişimini gösterir. Kuvvet değerleri iki farklı eksen için hesaplandıktan sonra numunenin fibere paralel ve dik yönlerdeki en kesit alanında bölgerek nominal gerilmeler ( $\sigma_i$ ) elde edilir. Burada düzlem için gerilme söz konusu olup  $i=1$  indis fibere paralel,  $i=2$  ise fibere dik gerilme bileşenini gösterir. Numunenin yatay eksenlerde yer değiştirmesi  $d_i = x_B(t) - x_{B_0}$ , (denklem 4'ten), birim şekil değişimi  $\varepsilon_i = \frac{d_i}{b}$ , uzama oranı ise  $\lambda_i = 1 + \varepsilon_i$  olur. Her iki yönde de numunenin en kesit genişliği  $b = 10$  mm ve kalınlığı ise  $t = 3$  mm olacak şekilde tendonlardan çıkartılmıştır. Daha sonra  $\sigma_i$  ve  $\lambda_i$  ölçümleri birlikte ele alınıp Ogden model eğrisine uydurularak modeldeki parametreler tespit edilmiştir.

benzer olduğu görülmüştür [22, 24].

Bir numuneye ait tipik ölçümler ve Ogden modelinden elde edilmiş gerilme-şekil değerlendirme eğrisi Şekil 5'te sunulmuştur. Ogden modelinin doğrulama sürecinde, düşük RMSE değerleri elde edilmiş ve bu da modelin çift eksenli Aşıl tendon biyomekaniği analizlerinde kullanılabilirliğini ortaya koymuştur. İlerleyen çalışmalarla, Ogden modelinin yanı sıra diğer hiperelastik modellerin karşılaştırılması ve farklı yükleme koşulları altında gerçekleştirilecek testlerle model performansının daha ayrıntılı incelenmesi önerilmektedir. Ayrıca, tendonun çift eksenli viskoelastik özelliklerinin belirlenmesi ve üç boyutlu gerilme-deformasyon analizlerinin yapılması, elde edilen sonuçların doğruluğunu artıracaktır. Bu çalışma, yumuşak doku mekanik karakterizasyonu ve biyomekanik modellemeler alanına önemli katkılar sunma potansiyeline sahiptir.

### 3. Sonuçlar



**Sekil 5.** Bir numune için elde edilen tipik ölçümeler ve Ogden modeliyle uydurulmuş eğrisi

**Figure 5.** A typical specimen's measurements and its fitted curve via Ogden model

### Yazar katklarının beyanı

SS: Tasarım, üretim, test, analiz, programlama, makale yazımı, SS makale yazımı. DT: Test, analiz, makale yazımı, CH: tasarım ve test, MP: yönetim, organizasyon, tasarım, test, analiz, programlama.

### Etki kurul onayı ve çıkar çatışması beyanı

Hazırlanan makalede etik kurul izni alınmasına gerek yoktur.

### Kaynaklar

- [1] Humphrey, J. D. (2003). Continuum biomechanics of soft biological tissues. *Proceedings of the Royal Society of London Series A*, 3–46. DOI:10.1098/rspa.2002.1060
- [2] Pereira, A. B., Fernandes, F. A. O., de Moraes, A. B., & Maio (2023). Biaxial Testing Machine: Development and Evaluation. *Machines*, 16. DOI:10.3390/machines8030040
- [3] Corti, A., Shameen, T., Sharma, S., De Paolis, A., & Cardoso, L. (2022). Biaxial testing system for characterization of mechanical and rupture properties of small samples. *Open Hardware Journal*, 20. DOI:10.1016/j.ohj.2022.e00333
- [4] Shiwartska, D. J., Tashman, J. W., Eaton, A. F., Apodaca, G., & Feinberg, A. W. (2020). 3D printed biaxial stretcher compatible with live fluorescence microscopy. *Zenodo*, 23. DOI:10.5281/zenodo.3483849
- [5] Sacks, M. S., & Sun, W. (2003). Multiaxial Mechanical Behavior of Biological Tissues. *Annual Review of Biomedical Engineering*, 5:251-84. DOI:10.1146/annurev.bioeng.5.011303.120714
- [6] Holzapfel, G. A., Gasser, T. C., & Ogden, R. W. (2000). A new constitutive framework for arterial wall mechanics and a comparative study of material models. *Journal of Elasticity and the Physical Science of Solids*, 1–3. DOI:10.1023/A:1010835316564
- [7] Lanir, Y., & Fung, Y. C. (1974). Two-dimensional mechanical properties of rabbit skin—I. *Journal of Biomechanics*, 29–34. DOI:10.1016/0021-9290(74)90067-0
- [8] Sun, W., Sacks, M. S., and Scott, M. J. (2005). Effects of Boundary Conditions on the Estimation of the Planar Biaxial Mechanical Properties of Soft Tissues. *ASME. J Biomech Eng.* 127(4): 709–715. DOI: 10.1115/1.1933931
- [9] Bell, E. D., Kunjir, R. S., & Monson, K. L. (2013). Biaxial and failure properties of passive rat middle cerebral arteries. *Journal of Biomechanics*, 91–96. DOI: 10.1016/j.jbiomech.2012.10.015
- [10] Horta Muñoz S, Serna Moreno MdC. Advances in Cruciform Biaxial Testing of Fibre-Reinforced Polymers. *Polymers*. 2022; 14(4):686. https://doi.org/10.3390/polym14040686
- [11] Ayyalasomayajula, V., & Skallerud, B. (2022). Microstructure and mechanics of the bovine trachea: Layer-specific investigations through SHG imaging and biaxial testing. *Journal of the Mechanical Behavior of Biomedical Materials*, 18. DOI:10.1016/j.jmbbm.2022.105371
- [12] Sacks MS. (1999). A method for planar biaxial mechanical testing that includes in-plane shear. *J Biomech Eng*. Oct;121(5):551-5. DOI: 10.1115/1.2835086. PMID: 10529924.
- [13] Sacks, M. S. (2000). Biaxial mechanical evaluation of planar biological materials. *Journal of Elasticity and the Physical Science of Solids*, 199. DOI:10.1023/A:1010917028671
- [14] Fung, Y. C. (1993). *Biomechanics: Mechanical Properties of Living Tissues*. Springer Science & Business Media. <https://www.proquest.com/legacydocview/EBC/3084753?accountid=10699>
- [15] Yang, G. (2008). *Strain Gauges for Biological Tissues* (Doctoral dissertation, University of California, Irvine). ProQuest Dissertations Publishing.
- [16] Schrininova S. (2024) Yumuşak dokunun biyomekanik karakterizasyonu için iki eksenli çekme-basma test cihazının geliştirilmesi. Yüksek Lisans Tezi, Ege Üniversitesi, Fen Bilimleri Enstitüsü.
- [17] Ozan, F, Okur, KT, Mavi, F, Pekedis M. (2025) Biomechanical and clinical assessment of dissociation in bipolar hip hemiarthroplasty. *Bio-Medical Materials and Engineering*. 36(3):185-199. doi:10.1177/09592989241306688.
- [18] Pekedis, M, Karaarslan, AA, Ozan, F, Tahta, M., Kayali, C (2025). Novel anchor-type proximal femoral nail for the improvement of bone-fixation integrity in treating intertrochanteric fractures: an experimental and computational characterization study. *Computer Methods in Biomechanics and Biomedical Engineering*, 1-17, DOI:10.1080/10255842.2025.2456985
- [19] Destrade M, Dorfmann L, Saccomandi G (2022). The Ogden model of rubber mechanics: 50 years of impact on nonlinear elasticity. *Philos Trans A Math Phys Eng Sci.* 380(2234):20210332. DOI: 10.1098/rsta.2021.0332.
- [20] Barroso, A., Correa, E, Freire J et al. (2018) A device for biaxial testing in uniaxial machines: design, manufacturing and experimental results using cruciform specimens of composite materials. *Exp Mech.* 58:49–53. DOI:10.1007/s11340-017-0327-6
- [21] Gupta, V., Gupta, S and Chanda A. Development of an ultra-low-cost planar biaxial tester for soft tissue characterization. *Biomed Phys Eng Express*. 2023;9(2). DOI:10.1088/2057-1976/acb940.
- [22] Samuel, S.S.T., Buckley P. C. and Zavatsky, A. B. (2016). Transverse Compression of Tendons. *ASME J Biomech Eng.* 138(4). DOI: 10.1115/1.4032627
- [23] Pekedis, M., Ozan, F., and Melez, M. (2025). Location-dependent biomechanical characterization of the human achilles tendon in diabetic and nondiabetic patients. *ASME J Biomech Eng.* 147(5): 051004. DOI: 10.1115/1.4068015
- [24] Khayyeri, H., Gustafsson A., Heijerjans A., Matikainen MK., Julkunen P., Eliasson, P., Aspenberg, P., Isaksson, H. (2015) A fibre-reinforced poroviscoelastic model accurately describes the biomechanical behaviour of the rat Achilles tendon. *PLoS One*. 1;10(6). DOI: 10.1371/journal.pone.0126869
- [25] Pekedis, M. (2025). In-vitro measurements coupled with in-silico simulations for stochastic calibration and uncertainty quantification of the mechanical response of biological materials. *arXiv [physics.med-ph]*, 1-28. DOI: 48550/arXiv.2503.09900

Dokuz Eylül Üniversitesi Mühendislik Fakültesi Fen ve Mühendislik Dergisi - Makale için kabul kararı verildi

8 Haziran 2025 13:52

Kimden: "DergiPark" <no-reply@mail0.dergipark.org.tr>

Kim'e: "mahmut pekedis" <mahmut.pekedis@ege.edu.tr>

**DİKKAT:** Bu e-posta kurum dışından gönderilmiştir. Zararlı dosya veya bağlantılar (link) içeriyor olabilir. Kaynağından emin olmadığınız dosyaları açmayın, bağlantılarına (link) tıklamayınız.

Şüpheli durumlarda lütfen Bilgi İşlem Daire Başkanlığı nyg.yardim@mail.ege.edu.tr adresine bilgi veriniz.

Ege Üniversitesi Bilgi İşlem Daire Başkanlığı, e-posta yoluyla kullanıcı ve şifre bilgisi **istememektedir**.

**Lütfen hiçbir koşulda parolanızı linklere tıklayıp yazmayınız!**

## DergiPark

AKADEMİK

Sayın Mahmut Pekedis,

1633531 - "Yumuşak Dokunun Biyomekanik Karakterizasyonu için iki Eksenli Çekme-Basma Test Cihazı" başlıklı makale için Yusuf Arman tarafından kabul kararı işaretlenmiştir.

Sayın Mahmut Pekedis,

Karar: Kabul Edildi

### Hakem Değerlendirmeleri

#### Hakem-1

1. Makale Kodu:

- 1633531

2. Makale Başlığı:

- Yumuşak Dokunun Biyomekanik Karakterizasyonu için iki Eksenli Çekme-Basma Test Cihazı

3. Makalenin türü:

- Araştırma Makalesi

4. 1. Makale başlığı çalışmayı yansıtıyor mu?:

- Evet

5. 2. Öz kısmı yazının amacını kapsamını yöntemini ve sonuçlarını içeriyor mu?:

- Evet

6. 3. İngilizce öz(abstract) Türkçe öz ile örtüşüyor mu?:

- Evet

7. 4. Giriş bölümünde çalışmanın amacı yeterince açıklanmış mı?:

- Evet

8. 5. Araştırmada kullanılan yöntem ve teknikler amaca uygun güncel ve yeterli midir?:

- Evet

9. 6. Araştırma yeni ve anlamlı veriler içeriyor mu?:

- Evet

# HECTOR SLAM BASED NAVIGATION WITH INTEGRATED OBJECT DETECTION

Saran SAPMAZ \*  
Mahmut PEKEDİS \*\*

**Abstract:** The main aim of this study is to develop an approach that detects and classifies objects in indoor areas by applying Hector Simultaneous Localization and Mapping (SLAM) and "You Only Look Once" (YOLO) algorithms to an autonomous, custom-made mobile robot. The approach is based on the Robot Operating System (ROS) and computer vision. The mobile robot's motion, path, and communication are controlled by the ROS navigation package. This paper provides a detailed description of the approach implemented to create a new map with objects, as well as information about the hardware and software configuration of the mobile robot. The object identification process and map creation are performed using a low-budget Laser Imaging Detection and Ranging (LIDAR) sensor and non-encoder DC motors. The results show that the proposed technique can detect objects with an accuracy of 97.8% and 94.86% for the x and y cartesian axes, respectively..

**Keywords:** Autonomous robot, Hector SLAM, ROS, YOLO

## Hector SLAM Based Navigation with Integrated Object Detection

**Özet:** Bu çalışmanın amacı iç mekanlarda Hector Eş Zamanlı Lokalizasyon ve Haritalama (EZLH) ve "Sadece Bir Defa Bak" (SBDB) kullanan özel yapım bir otonom robotun nesneleri algılamasını ve onları sınıflandırmamasını sağlayan bir yaklaşım geliştirmektir. Yaklaşım, Robot İşletim Sistemi (RİS) ve bilgisayarla görme teknolojilerine dayanmaktadır. Mobil robotun hareketi, izlediği yolu ve iletişim, RİS navigasyon paketiyle kontrol edilmektedir. Makale, yeni bir harita oluşturmak için uygulanan algoritmanın ayrıntılı bir açıklamasının yanı sıra, mobil robotun donanım ve yazılım yapılandırmasına ilişkin bilgileri de sunmaktadır. Nesne tanımlama süreci ve harita oluşturma, düşük bütçeli bir Lazer Görüntüleme Algılama ve Mesafe Ölçümü (LGAMÖ) sensörü ile enkodersiz direkt akım (DA) motorlar kullanılarak yapılmaktadır. Sonuçlar, önerilen tekniğin nesneleri sırasıyla x ve y kartezyen eksenlerinde % 97,8 ve % 94,86 doğrulukla tespit edebildiğini göstermektedir.

**Anahtar Kelimeler:** Otonom robot, Hector Eş Zamanlı Lokalizasyon ve Haritalama (EZLH), Robot İşletim Sistemi (RİS), Sadece Bir Defa Bak (SBDB)

## 1. INTRODUCTION

The number of algorithms deployed for robots has increased over time as robots have become more accessible to everyone. Most of these algorithms are available to the public so that other developers can take advantage of these open-source tools and develop their own algorithms. Simultaneous localization and mapping (SLAM) is one of the open-source tools and is applied to

---

\* Yazar 1 İletişim Adresi (Ege Üni., Fen Bilimleri Enstitüsü, Makine Müh., Ziraat Fakültesi Prof. Dr. Necdet BUDAK Blogu Kat:3 Bornova - İzmir)

\*\* Yazar 2 İletişim Adresi (Ege Üni., Mühendislik Fakültesi, Makine Müh., Erzene Mahallesi, Ege Ünv. No:172, 35040 Bornova/İzmir)

İletişim Yazarı: Saran Sapmaz (saran.sapmaz1@gmail.com)

create a map of an unknown environment by simultaneously locating the position of the robot (Blas and Riisgaard, 2005). The ability to create a map in the absence of GPS makes SLAM popular. Over the decades, researchers have used different sensors, cameras, or a combination of both to create maps and localize robots. One of these techniques is Hector SLAM, and this technique spends fewer resources than other algorithms such as gmapping and cartographer because odometry information is not required for map creation and localization in Hector SLAM. Instead, laser streams are used to position the robot within the map using specific configuration files for navigation (Kohlbrecher and Meyer, 2010). These files include properties of the custom robot, expected trajectory, sensor configuration, and ROS topics to execute the navigation (Marder-Eppstein, 2010). Hector SLAM processes in ROS (Robot Operating System) that are used by robotic field researchers to control various robots using standard, ready-to-use algorithms. It is not an actual OS like Windows but an interface-like system that works with Linux-based operating systems (O’Kane, 2014).

While Hector SLAM provides robust mapping and localization, its primary output is a geometric map. For some autonomous robotic applications, understanding the objects within the environment is required. This setup can be used in hazardous indoor areas with different custom robots for exploration purposes. The custom-built robot can have any 2D LiDAR sensor that can publish information. In 2018, researchers compared various SLAM techniques with and without camera information. They categorized them into (a) 2D lidar-based: GMmapping, Hector SLAM, Cartographer; (b) monocular camera-based; and (c) stereo camera-based. In their comparative study, Filipenko and Afanasyev (2018) tested three 2D LiDAR SLAM systems: GMmapping, Hector SLAM, and Cartographer. They reported that GMmapping did not provide reliable results. A key finding in their analysis was the comparison between the trajectories generated by Hector SLAM and Cartographer. Their evaluation using Absolute Trajectory Error (ATE) metrics showed that the Root Mean Square Error (RMSE) between these two trajectories was less than 3 cm. This led them to conclude that both systems produce practically the same results. In our work, we focus on Hector SLAM, which falls under the category of 2D LiDAR-based techniques. It stands out due to its low resource consumption and the fact that it does not require odometry. Hector mapping costs less CPU than other mapping techniques such as gmapping and cartographer. Hector SLAM depends only on sensor information to create a map, while gmapping requires additional odometry information. Another popular SLAM technique, Cartographer, requires at least 16GB of RAM (Filipenko and Afanasyev, 2018).

SLAM is sufficient for gathering information about the indoor area, but the addition of a camera to the system allows for gathering even more data and a better understanding of the area. The LiDAR sensor, which is one of the most utilized sensors, allows for the creation of a detailed map of its surroundings and the avoidance of obstacles in real-time. The robot can accurately navigate its environment with the help of the LiDAR sensor by using the ROS navigation package and SLAM techniques (Hess et al., 2016). Moreover, the camera can be used as an extra sensor in the system to improve SLAM (Chghaf, 2022, Sapmaz, 2022). In 2015, Kamarudin and his colleagues compared popular SLAM techniques with and without a camera. One of the interesting findings is that a camera without using a sensor failed the SLAM process; however, a sensor without a camera succeeded in performing it. Moreover, when both the camera and the sensor are utilized for performing SLAM, the map becomes more detailed. The work concludes that the camera may improve SLAM performance (Kamarudin et al., 2015). Another approach to camera usage with SLAM may be utilized to recognize objects with computer vision simultaneously but as a separate process. This approach allows the camera to independently identify objects while SLAM focuses on map creation and robot localization. In 2019, Kashi and his colleagues developed an algorithm using gmapping (a SLAM technique) and a computer vision algorithm to create a map with recognized objects simultaneously. The camera has not been utilized directly to create a map but only to recognize objects (Kashi, Sriram, and Mohan, 2019). On the other hand, Hector SLAM is constrained with this approach since it cannot work with Python 3-

dependent OpenCV libraries on ROS Kinetic (Fairchild and Harman, 2017) but only with the “find\_object\_2d” ROS package. As a result of this constraint, other methods have been developed by researchers. One of the methods is asynchronous, with map creation and image processing being performed independently or at different times. In the literature, utilizing Python 3-dependent OpenCV libraries with the Hector SLAM algorithm has been implemented by Hakim and his colleague in 2019. The object recognition has been implemented with YOLO (Fadhil and Hakim, 2019).

In this paper, an approach has been developed as we have not been interested in using the mentioned ROS package as a source of object recognition. Also, it has been applied to a custom-made autonomous robot whose motion has been provided by the navigation stack. The localization of the objects relies on the correct calculations of transformation and rotation matrices. Hector SLAM focuses on processing the map and implicitly navigating the robot as the camera takes pictures and stores them for processing purposes.

This paper presents an approach that combines Hector SLAM and computer vision using YOLO to detect objects and visualize them on another map on ROS Kinetic. We developed a custom mobile robot entirely from the scratch up and successfully deployed our algorithm on it. The robot is built using cost-effective reliable sensors and low-PWM, high-torque DC motors, providing a robust platform for experimentation. A Raspberry Pi 3B+ and an Arduino serve as the primary microcontrollers, interfaced via USB and integrated through a Robot Operating System (ROS) communication protocol, the details of which are discussed later in this paper. A key finding of our work is the successful demonstration of object detection and map generation without the need for odometry data.

## 2. METHODOLOGY

### 2.1. Hardware and Mechanical Design

The mobility The mobility of the custom mobile robot is provided by two differential wheels and one caster wheel. The robot consists of two lightweight wooden chassis. The lower part includes an L298N motor driver, an Arduino UNO microcontroller, and a power bank. The upper part consists of 8 batteries, a Raspberry Pi 3B+, a camera, and a LIDAR sensor. We chose the Raspberry Pi 3B+ model over the 4 because it is more cost-effective and sufficient for our algorithm's demands. Its primary function is to publish sensor data and images as a ROS stream. Due to its 1GB SDRAM, it is incapable of executing the algorithm simultaneously on its own and requires a connection to a more powerful machine for processing. However, it is possible to create communication through both 2.4GHz and 5GHz WiFi networks. The communication between the Raspberry Pi and the Ubuntu laptop was provided over the same IP. The Raspberry Pi is powered by an 11500 mAh power bank with a constant 2A output ampere and 5V output voltage, which is connected to the Pi using a USB cable. The Arduino and LIDAR are powered by the Raspberry Pi using compatible USB cables. The DC motors are connected to the output pins of the L298N motor driver, and the input pins of the motor driver are connected to the Arduino. The motor driver is powered by 8 pieces of 1.1V batteries in series (Fig. 1).

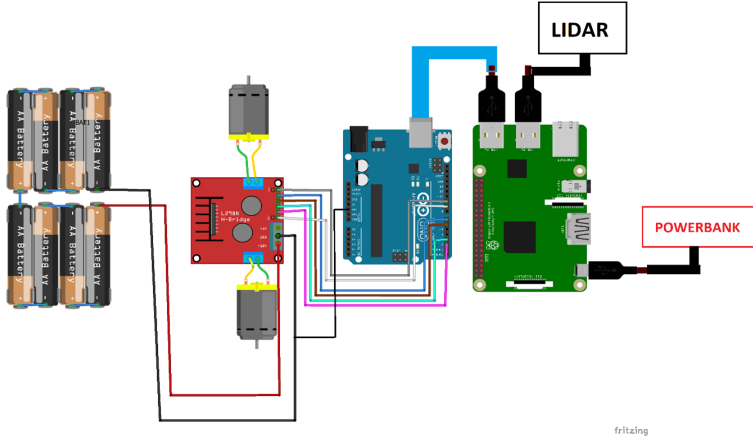


**Figure 1:**  
Connection diagram of the mobile robot.

Two parts of the robot are designed on a CAD program for purposes of both simulation and real-life application. The chassis is manufactured using 3mm thick lightwood material as it is easy to cause necessary deformations without breaking it and is lighter than PLA material, which is generally used for 3D printers. The holder of the DC motor is an L-shaped connector that links the motor to the chassis. As extra deformation is not required, PLA material is used. The most important part of the mobile robot is the placement of the LiDAR sensor, as its 0th degree indicates the x-axis for the algorithm to work. The axes of the camera and LiDAR should be arranged to be in the same orientation. Therefore, the LiDAR was mounted in the same direction as the camera.

## 2.2. Software

A Raspberry Pi with Raspbian Stretch OS and a laptop with Ubuntu OS have been used to operate ROS Kinetic. The codes inside the Raspberry Pi were executed using the SSH protocol, which allows for remote control without the need for an external monitor to access its terminal. Performing SLAM and taking pictures simultaneously has been processed on the Ubuntu laptop. The Raspberry Pi has been set to be a ROS Master provider. ROS packages for the camera, sensor, and Arduino have been installed in the Raspberry Pi's ROS workspace to convert raw data into ROS topics. The connection between Arduino and ROS Master is provided to control the mobility of the robot. Similarly, relevant ROS packages such as Hector SLAM and the navigation stack have been installed on the laptop for SLAM processes.

RViz is an application that visualizes sensor data with its own tools, which can publish ROS topics or subscribe to existing ROS topics (Hyeong et al., 2015). The application creates a map by subscribing to ROS topics that the Hector SLAM technique publishes as the robot moves indoors. The navigation tool of RViz can be used to point to anywhere on the map and publish desired orientation information for the robot, since the motion depends on the navigation stack. The computer vision algorithm YOLO can only be used with Python 3 and OpenCV libraries. A separate virtual environment was created on the Ubuntu laptop that depends on Python 3 to perform object recognition. Object recognition has been carried out in a virtual environment with Python 3 installed using a computer vision algorithm. YOLO is designed to detect objects at three different scales—small, medium, and large—with respective scales of 32, 16, and 8 pixels. This allows the algorithm to detect objects of varying sizes with high accuracy (Bisallah et al., 2016).

### 2.3. Algorithm

A connection is established between an Ubuntu 16.04 laptop and a Raspberry Pi over the same IP address. The IP addresses are specified on two lines within the .bashrc files for both machines. On the Raspberry Pi's .bashrc file, both IP values are set to the Raspberry Pi's IP address. The Ubuntu laptop has a similar .bashrc file. The Master IP is set to the master's IP address, and the other IP value is set to the Ubuntu laptop's IP address. Then, both files are saved, and the source command is used in the terminal to apply these values permanently. This technique enables these devices to communicate over one ROS master.

The algorithm consists of two main launch files and four Python codes. Fig. 2 shows the brief algorithm scheme of these codes. Raspberry Pi 3B+ has 1GB of SDRAM, and it is not possible to process this data quickly every time due this limited memory. Therefore, a ".launch" file has been written for the Raspberry Pi 3B+. Launch files are ".xml" type files that include one or more executable nodes. The first launch file is executed on the Raspberry Pi and consists of three main tasks: publishing sensor stream, publishing camera stream, and establishing communication between Arduino and ROS. It is executed using SSH through the laptop. The second launch file on the laptop, which has three main tasks, is executed using the terminal of Ubuntu. These tasks are starting the RViz application with pre-configuration, subscribing to the sensor stream and executing both the Hector SLAM, and the navigation stack. It subscribes to ROS topics published by SLAM and the sensor stream, and publishing the required velocity.

The navigation is provided by an external node called "explore\_lite." The mobile robot moves until all frontiers are cleared. This node subscribes to "map\_msgs/OccupancyGridUpdate" and "nav\_msgs/OccupancyGrid" messages published by Hector SLAM. These messages contain information about the updated and the full map. Then, the "explore\_lite" node defines the direction of movement based on the map and its updates. For the mobile robot's movement, the "cmd\_vel" topic is passed to the "move\_base" topic. Simultaneously, the Arduino subscribes to the "cmd\_vel" topic and uses the "geometry\_msgs/Twist" message data to set the PWM values for the DC motors. Meanwhile, "move\_base" utilizes the "cmd\_vel" commands to plan and control the robot's movement for navigation. Finally, "move\_base" publishes the "geometry\_msgs/PolygonStamped" message that is utilized by "explore\_lite" to complete the cycle of exploration.

The LiDAR sensor publishes a "scan" topic that contains information on 360 distance measurements per 1 degree. The Pi camera streams an "image\_raw" ROS topic. The relations between the frames of the independent parts of the robot and the map are published by the "tf" topic. The position of the robot is established by the "slam\_out\_pose" topic. Our algorithm starts by subscribing to these ROS topics. The main goal is to find the position of any obstacles in the real-world frame. The "tf" ROS topic is used to track frames between the robot's chassis, "base\_link," and the "map" itself. It broadcasts information about translation in x, y, z coordinates (in meters) and rotation (in quaternions) between specified frames. This information is used to determine the possible position of obstacles by using transformation matrices combined with the distance of the obstacle from the 'scan' topic. We positioned the sensor's zeroth degree to face forward and defined our area of interest as -10° to 10°. Our aim is to find the minimal distance and its corresponding angle relative to the robot's base, as published by the 'scan' topic within this specified area. The acceptable distance range for obstacle detection was determined to be between 0.4 and 1 meter through trial and error. This range was chosen because the photo quality degraded at closer ranges than 0.4 meters, and the number of detected objects increased at distances beyond 1 meter. Once an obstacle falls within the 0.4 to 1 m range, the algorithm identifies the minimum distance and its corresponding angle. These define the possible obstacle's position with respect to the robot's frame. This information is then conveyed into transformation matrices to acquire the obstacle's position with respect to the map. The main aim is to determine the position of the robot on the map frame, which is initially unknown.

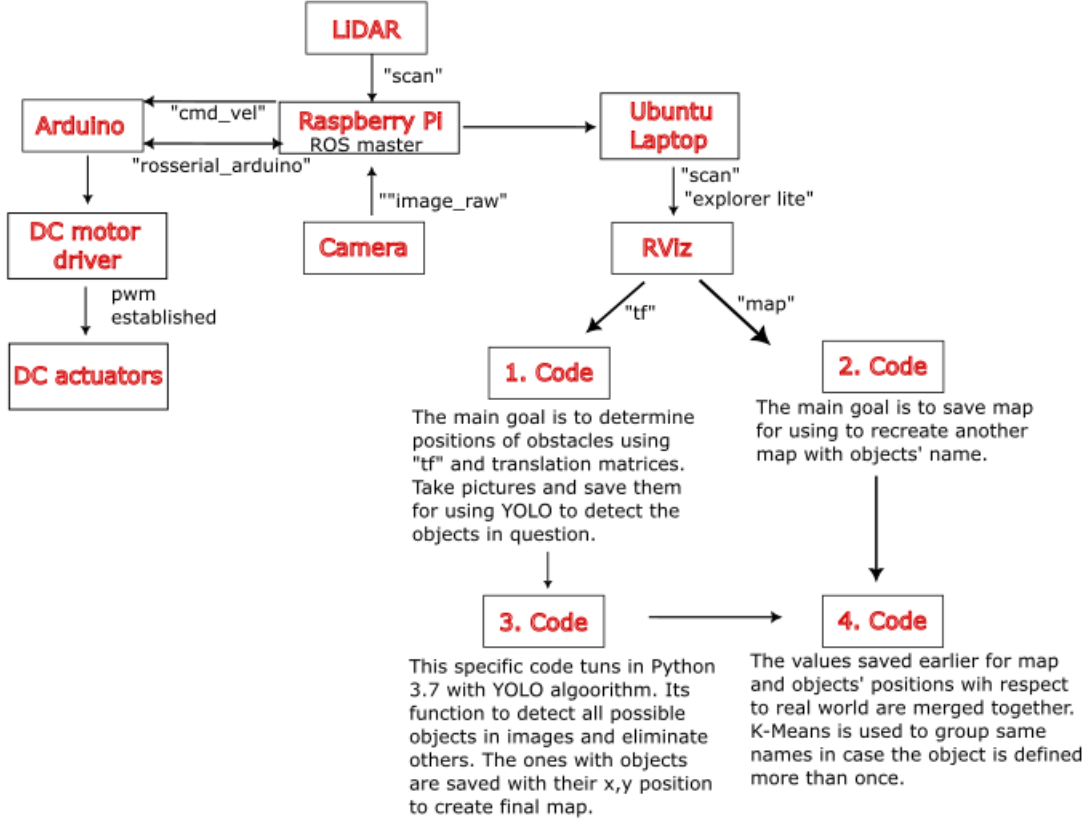


**Figure 2:**

The brief algorithm scheme illustrates connections between ROS and mechanical design.

The x-axis of the robot frame depends on how the LiDAR is mounted. The first and second elements of the measurement array define the x-axis and y-axis of the robot, respectively. The frame of the robot moves on RViz with respect to the map frame as the robot roams around. The x-axis of the map frame is defined as the x-axis of the robot's initial orientation when the SLAM process begins, and this frame remains fixed until the end of the process (Fig. 3).

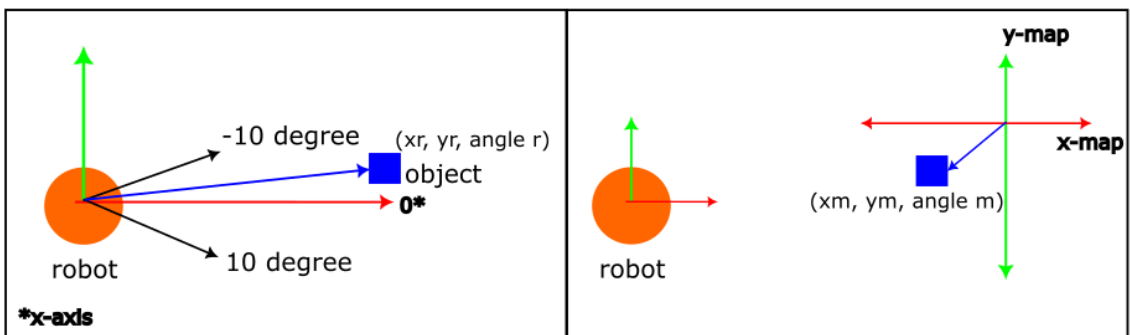


**Figure 3:**

The logic behind transformation matrices.

The first step is to locate the obstacle on the robot frame as a pair coordinate of  $(x_r, y_r)$ ,

$$x_r = d \cos (\theta_r) \quad (1)$$

$$y_r = d \sin (\theta_r) \quad (2)$$

where the obstacle distance ( $d$ ) is defined by the minimum value among the collected 20 samples from of LiDAR in range -10 to 10 degrees. The angular resolution of the sensor is 1 degree, and it can collect 360 measurements. The x-axis of the LiDAR is assumed to be 0 degrees. Using the right-hand rule, degrees between -10 and 10 can be determined. We have limited the data collection by not processing each measurement. The angle of an object with respect to the robot frame is a value between -10 and 10, represented as  $\theta_r$ . If  $\theta_r$  is between -10 and -1 degrees,  $y_r$  is multiplied by -1 for equation (2) as y point should be exact negative.

The next step is to find where the robot is located with respect to the map frame. As the robot frame translates and rotates on the RVIZ screen, unique transformation matrices are published by the ROS tf package for each frame. The transformation matrix quantifies the displacement of the robot frame relative to the map frame due to the robot's motion. This matrix contains information about the amount of translation and rotation of the robot frame relative to the map frame. In this step, the values of  $x_r$ ,  $y_r$  have been calculated. Pair of ( $x_t$ ,  $y_t$ ) and the amount of rotation  $\varphi$  (in quaternion) are published by "tf" ROS topic. The first step is to apply the rotation matrix to the known  $x_r$ ,  $y_r$  points.

$$R = \begin{bmatrix} \cos\varphi & -\sin\varphi & 0 \\ \sin\varphi & \cos\varphi & 0 \\ 0 & 0 & 1 \end{bmatrix} \begin{bmatrix} x_r \\ y_r \\ 1 \end{bmatrix} \quad (3)$$

$$R = \begin{bmatrix} \cos\varphi * x_r - \sin\varphi * y_r \\ \sin\varphi * x_r + \cos\varphi * y_r \\ 1 \end{bmatrix} \quad (4)$$

where  $R$  defines the position of obstacle in rotated frame amount of  $\varphi$  degree.

The next step is to apply matrix  $T$  to  $R$  (Craig, 2014)

$$T = \begin{bmatrix} 1 & 0 & -x_t \\ 0 & 1 & -y_t \\ 0 & 0 & 1 \end{bmatrix} \cdot R \quad (5)$$

$$T = \begin{bmatrix} \cos\varphi * x_r - \sin\varphi * y_r - x_t \\ \sin\varphi * x_r + \cos\varphi * y_r - y_t \\ 1 \end{bmatrix} \quad (6)$$

where  $T$  matrix represent the robot location with respect to the map frame which are  $x_m$  and  $y_m$ . Equations 1-4 are embedded into the algorithm to determine the possible positions of obstacles. This pair of ( $x_m$ ,  $y_m$ ) coordinates is saved into a pickle file with image names to process later. As soon as the LiDAR sensor detects an obstacle within the specified distance range (0.4m to 1m), an image is captured. Prior to any processing, the image data from the 'image\_raw' ROS topic is converted into a Computer Vision (cv) format, which is compatible with Python's image processing libraries. The second Python code is activated after the exploration process is complete. Its aim is to save the final map as a list of ( $x$ ,  $y$ ) coordinate pairs within a pickle file. The 'map' ROS topic provides information about the final map as a 1024x1024 matrix. This matrix uses the following values: 0 for explored and unoccupied areas, -1 for unexplored areas, and 1 for explored and occupied areas. This code specifically extracts the ( $x$ ,  $y$ ) coordinates corresponding to the value '1' to create a usable final map representation for the next processing. For a more detailed workflow, please refer to supplementary material 1.

The third and fourth Python codes were executed with Python 3.7 (Fig. 4). To run these codes, a virtual environment was set up on Ubuntu 16.04, and this virtual environment was made compatible with Python 3.7. The third Python code executes an object recognition algorithm

(YOLO) by filtering each image recorded in the first Python code one by one. Within this code, first, the 'pickle' file obtained from the first code is opened. Inside the 'pickle' file, there are x, y coordinates and file paths. The images within the file paths are sent to the method where the image processing algorithm starts, along with their x and y coordinates. For each photograph sent, if an object is detected in the photograph, the x and y coordinates corresponding to the file path and the names of the objects are added to separate matrices. If no object is detected, no action is taken. All matrices are first saved in dictionary format. This dictionary is then converted back into a 'pickle' file. The fourth Python code, on the other hand, is the code where the map information coming from RViz is combined with the object names and object coordinate information coming from the algorithm. Additionally, since the same object can be detected multiple times, it performs cluster grouping for a single object using k-means. By definition, the k-means clustering algorithm groups data points into clusters by minimizing the distance between each point and its cluster's centroid.

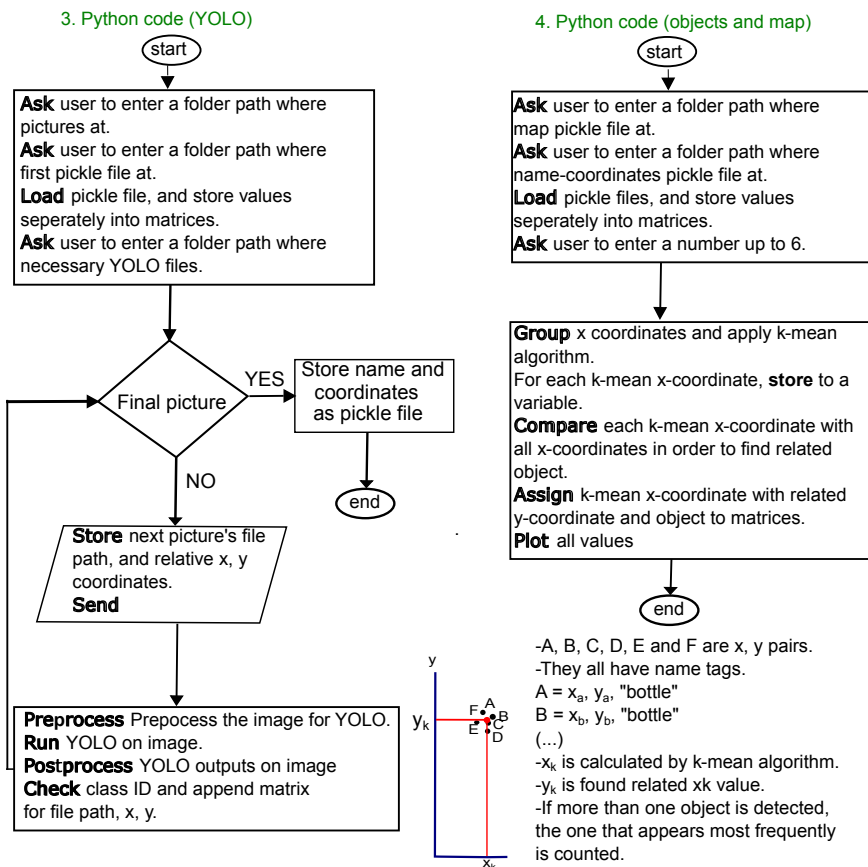


**Figure 4:**  
The flowchart of third and fourth Python codes.

### 3. RESULTS

The algorithm has been tested in two different places that were accurately recognized 18 of 20 objects, resulting in a detection accuracy of 90 %. Positioning error was calculated comparing points that the algorithm had returned with real x, y (m) values which were distances of objects' point (0, 0) to nearest wall/obstacle. For area calculation, we used the longest dimensions of the regions, treating them as rectangular approximations. This method was applied to both the map

obtained in RViz and the real-life areas. Each object has its imaginary frame. The false positioning of the objects is calculated as pair of x, y %, and overall result is calculated as 2,2%, 5,14%.

In the 1st room, two bottles were recognized correctly. The room, and a typical map created by the algorithm can be seen in Fig. 5. Blue dots represent obstacles and objects. Additionally, purple dot is the object detected by algorithm, and red dot shows reference point (0,0) of the map.



**Figure 5:**  
The first room with bottles and its final map;  
**a.** The indoor **b.** The map

Table 1 shows the x and y values calculated by the algorithm and ground truth (exact) observations. For the first object, the exact coordinates are (1.79, 0.72) m, and for the second object, they are (1.3, 0.72) m. The accuracy of the x and y values for the first object are 97.02% and 90.8%, respectively. For the second object, it is 96.82% for x and 95.1% for y.

**Tabel 1. Distance errors for the 1st room.**

Case	Object 1 (x, y) m	Object 1 Error x%, y%	Object 2 (x, y) m	Object 2 Error x%, y%
1	(1.75, 0.78)	2.2, 8.3	(1.3, 0.72)	0, 0
2	(1.76, 0.64)	1.6, 11.1	(1.23, 0.76)	5.3, 8.3
3	(1.66 , 0.67)	7.2, 6.9	(1.34 , 0.67)	3, 6.9
4	(1.76, 0.62)	1.7, 13.9	(1.23, 0.72)	5.3, 6.9
5	(1.75, 0.68)	2.2, 5.8	(1.269, 0.738)	2.3, 2.4

The ground truth (true) location of the the 1<sup>st</sup> object is (1.79, 0.72) m, and 2<sup>nd</sup> object is (1.3, 0.72) m.

Furthermore, the identification success of the algorithm is 80 % for the second room. The 2<sup>nd</sup> room and a typical map created by the algorithm is given in Fig. 6.

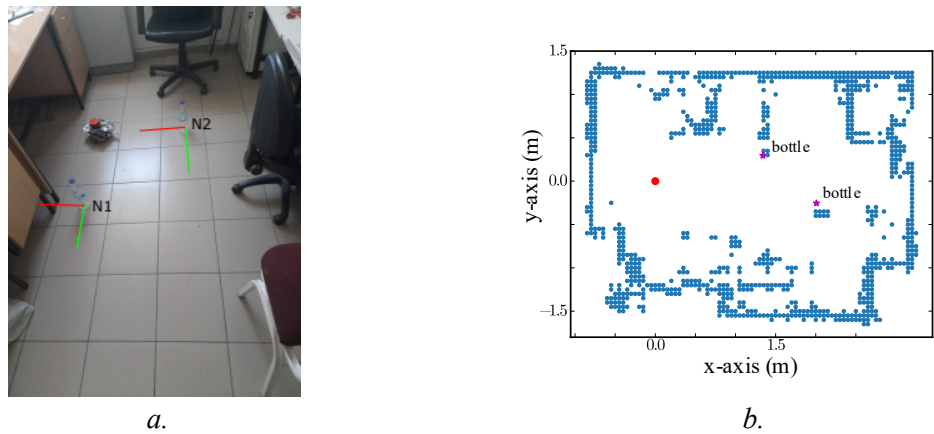


**Figure 6:**  
The second room with bottles, books and its final map;  
**a.** The indoor **b.** The map

The results observed for the 2<sup>nd</sup> room are summarized in table 2. The ground truth location of the first and second objects are (0.94, 2.1) m and (1.2, 1.2) m, respectively. The average identification scores for the first and second object are 97.59% and 94.86%, respectively.

**Table 2. Identification scores of the algorithm observed for the 2nd room.**

Case	Object 1 (x, y) m	Object 1 Error x%, y%	Object 2 (x, y) m	Object 2 Error x%, y%
1	(0.95, 2.13)	1, 1.6	(1.52, 1.18)	26.6, 1.6
2	(0.94, 2.13)	0, 1.6	(1.2, 1.3)	0, 8.3
3	(-, -)	-, -	(1.18, 1.15)	1.6, 4.16
4	(-, -)	-, -	(1.23, 1.19)	2.5, 0.8
5	(0.88, 2.18)	6.38, 3.8	(1.14, 1.21)	5, 0.83

The ground truth (true) location of the the 1st object is (0.94, 2.1) m, and the 2nd object is (1.2, 1.2) m.

The overall MSE scores for the x and y coordinates found by the algorithm across 18 takes are 0.00855 and 0.00271, respectively.

#### 4. DISCUSSION

This research presents a cost-effective mobile robot for mapping, object localization, and detection. We have deployed a wide variety of tools such as the LIDAR sensor, actuators, a high-resolution camera, motors, Arduino MPU, and Raspberry Pi CPU. The communication between hardware components was performed using ROS on the open-source Ubuntu operating system. The investigations were conducted at two sites, and the following results were obtained.

In the first stage, we investigated how well the SLAM algorithm can generate the actual maps, visualize them, and compute their area. The overall results obtained in our study are as follows. First, the algorithm can compute the area of the first and second rooms with high scores of 4.49% and 4.48%. In the second stage, the goal was to identify how well the algorithm can detect the objects. The results show that the average correct identification of the objects is 85%. The slight errors could be due to image resolution and lighting. Finally, we investigated whether the

proposed approach could determine the location of the object as an addition to the detection process. The results showed that the approach could locate the object with an average performance of 95.5%. We expect that the errors between the ground truth and the values computed by the algorithm may be due to the sensitivity of the LIDAR.

In their 2024 work, Chowdhury and Houssain implemented Hector SLAM for indoor navigation with obstacles, using a camera to capture obstacle images (Chowdhury and Houssain, 2024). While successful in rectangular environments, their approach was not tested with randomly shaped places, and they did not incorporate obstacle mapping as we have done in our study. Furthermore, unlike their method which utilized an additional IMU for position correction, we chose not to implement extra odometric information for defining the robot's and obstacle's positions. In their 2019 paper, Kashi and his team developed an interesting algorithm that used Gmapping (a SLAM method) along with computer vision to build a map while also identifying objects. Interestingly, much like our own study (Kashi, Sriram, and Mohan, 2019), they didn't use the camera to directly create the map, but specifically for recognizing objects. They successfully took pictures of obstacles and labeled them in Rviz. They also used a hall effect sensor to get the robot's position, as Gmapping needs external odometry data. However, their testing was limited to just one environment. Also, they didn't include the actual positions of the obstacles, either in Rviz or real-world data, for comparison. Their main focus was on how confident they were in identifying the objects. In the literature, utilizing Python 3-dependent OpenCV libraries with the Hector SLAM algorithm has been implemented by Hakim and his colleague in 2019. The object recognition has been implemented with YOLO. They developed a smart stick for people with impaired vision. They created a map of the environment using Hector SLAM and then applied a computer vision algorithm to recognize objects. The objective is to establish a pathway that would let individuals navigate without encountering obstacles and provide them with information about their environment (Fadhil and Hakim, 2019). However, they haven't developed their algorithm using an autonomous mobile robot and haven't taken pictures simultaneously as their stick moves around. Different from the mentioned studies, we include object identification processes, and the results are promising. We expect that the methodology we suggest can be applied in various applications, such as object identification and localization in hazardous areas where humans cannot access.

Although the performance of the approach is reasonable, this study is not without limitations. Firstly, the investigation was carried out in indoor rooms with sunlight. Future studies could extend the approach to sites with limited lighting. Secondly, the scanning time duration for a 4 m<sup>2</sup> indoor room is approximately 10 minutes with this version of the robot. This duration could be shortened by modifying the hardware, software, and mechanical design. Thirdly, the approach was tested in a human living room. Additional studies could be implemented to investigate its sensitivity in hazardous areas. The current version of the robot operates on a Wi-Fi connection, whose sensitivity can decrease with distance. To localize sites remotely over greater distances, the connection could be made via radio communication. The transformation and rotation matrices are implemented correctly in the system, as the error values remain consistent, with only a few variations observed in certain results. Moreover, the navigation stack is utilized with custom-made values to navigate the system, ensuring unique parameters for each project. Since it is a frame-based system, the replacement of the laser scanner holds significant importance. In this paper, to simplify the process, the x-axis of the laser scanner has been selected, and all calculations are performed relative to this specific axis.

## 5. CONCLUSION

In this study, a mobile robot was built with the ability to move on its own, recognize objects, and understand its surroundings. The robot's control and computing parts communicated in real time using the Robot Operating System (ROS). It used the YOLO (You Only Look Once) method

to recognize objects and SLAM (Simultaneous Localization and Mapping) to figure out where it was and to map the area around it. During testing, it was noticed that sometimes the robot finished mapping before it could detect certain objects. To solve this, an interactive tool was used so users could click on a location, and the robot would move there on its own to take pictures.

In conclusion, this robot offers a budget-friendly alternative to expensive commercial systems, and it can perform important tasks like mapping, finding its location, and recognizing objects. Thanks to Hector SLAM, it can accurately figure out where it is without needing extra location tools. The results show that this method could work well for indoor robot tasks. Future work will focus on testing the robot in more challenging and risky real-world settings.

## CONFLICT OF INTEREST

The author(s) confirm that there are no known conflicts of interest or shared interests with any institution, organization, or individual.

## CONTRIBUTIONS OF AUTHORS

Saran Sapmaz data collection, data analysis, and writing the article, Mahmut Pekedis workflow design and data visualization.

## REFERENCES

1. [https://dspace.mit.edu/bitstream/handle/1721.1/119149/16-412j-spring-2005/contents/projects/1aslasm\\_blas\\_repo.pdf](https://dspace.mit.edu/bitstream/handle/1721.1/119149/16-412j-spring-2005/contents/projects/1aslasm_blas_repo.pdf), Date of Access: 07.06.2023, Topic: *Blas MR and Riisgaard S (2005) SLAM for Dummies: A Tutorial Approach to Simultaneous Localization and Mapping*.
2. Kohlbrecher, S., Meyer, J., Stryk O. von and U. Klingauf (2011), A flexible and scalable SLAM system with full 3D motion estimation, *Proc. IEEE International Symposium on Safety, Security and Rescue Robotics (SSRR)*, 155-160, doi: 10.1109/SSRR.2011.6106777.
3. Marder-Eppstein, E. et al. (2010), The office marathon: robust navigation in an indoor office environment, *International Conference on Robotics and Automation*, 300-307, doi: 10.1109/ROBOT.2010.5509725
4. <https://jokane.net/agitr/agitr-letter.pdf>, Date of Access: 06.06.2023, Topic: A Gentle Introduction to ROS.
5. Chghaf, M.R. (2022), Camera, lidar and multi-modal SLAM systems for autonomous ground vehicles: a survey, *Journal of Intelligent & Robotic Systems*, volume (105):2. DOI: 10.1007/s10846-022-01582-8
6. Sapmaz, S. (2022), Yumuşak dokunun biyomekanik karakterizasyonu için iki eksenli çekme-basma test cihazının geliştirilmesi, M. Sc. Thesis, Ege University, TR.
7. K. Kamarudin *et al.* (2015), Improving performance of 2D SLAM methods by complementing Kinect with laser scanner, *2015 IEEE International Symposium on Robotics and Intelligent Sensors (IRIS)*, Langkawi, 278-283, doi: 10.1109/IRIS.2015.7451625.

8. Kashi, M.S, Sriram, T.B. and Mohan, R. (2019), An Approach to labelled indoor mapping using SLAM and object detection. *2019 IEEE Region 10 Symposium (TENSYMP)*, 321-325. DOI: 10.1109/TENSYMP46218.2019.8971298
9. [https://sceweb.sce.uhcl.edu/harman/CENG5437\\_MobileRobots/Webitems2020/ROS\\_ROBOTICS\\_BY\\_EXAMPLE\\_SECOND\\_EDITION.pdf](https://sceweb.sce.uhcl.edu/harman/CENG5437_MobileRobots/Webitems2020/ROS_ROBOTICS_BY_EXAMPLE_SECOND_EDITION.pdf), Date of Access: 07.06.2023, Topic: *ROS Robotics By Example-Second Edition*. Leeds: Packt.
10. Fadhil A. and Hakim H. (2019) Indoor low cost assistive device using 2D SLAM based on LIDAR for visually impaired people, *Iraqi Journal of Electrical and Electronic Engineering* (15)2: pp 115-121.
11. M. Filipenko and I. Afanasyev (2018). Comparison of Various SLAM Systems for Mobile Robot in an Indoor Environment. In 2018 International Conference on Intelligent Systems (IS), pp. 400-407. doi: 10.1109/IS.2018.8710464.
12. Hess, W., Kohler, D., Rapp, H. and Andor, D. (2016), Real-Time loop closure in 2D LIDAR SLAM, *2016 IEEE International Conference on Robotics and Automation (ICRA)*, pp: 1271-1278.
13. Hyeong, R.K., Lee, S., Park, T. and Kim, C. (2015) RViz: a toolkit for real domain data visualization, *Telecommunication Systems* (60): 337-345, doi: 10.1007/s11235-015-0034-5
14. Bisallah, H.I., Oguin, K.J. and Oguine, O.C. (2022), YOLO v3: Visual and Real-Time Object Detection Model for Smart Surveillance Systems(3s), doi: 10.48550/arXiv.2209.12447
15. Craig, J.J. (2014), *Introduction to Robotics Mechanics and Control (3 ed.)*, Leeds: Pearson Education Limited.
16. Hossain, A. and Chowdhury, R.H. (2024) "Implementation of Hector SLAM Algorithm for Mapping Indoor Environments with Obstacles," *2024 IEEE 3rd International Conference on Robotics, Automation, Artificial-Intelligence and Internet-of-Things (RAAICON)*, Dhaka, Bangladesh, 2024, pp. 218-223, doi: 10.1109/RAAICON64172.2024.10928605.



## [Dergipark] Yeni Bildiriminiz var / You have new notification

27 Haziran 2025 16:25

Kimden: "DergiPark" <no-reply@mail0.dergipark.org.tr>

Kime: "mahmut pekedis" <mahmut.pekedis@ege.edu.tr>

**DİKKAT:** Dış resimler görüntülenmez. Resimleri Görüntüle

Şundan gelen mesajları her zaman görüntüle mail0.dergipark.org.tr ya da no-reply@mail0.dergipark.org.tr



**DİKKAT: Bu e-posta kurum dışından gönderilmiştir. Zararlı dosya veya bağlantılar (link) içeriyor olabilir. Kaynağından emin olmadığınız dosyaları açmayın, bağlantılarla (link) tıklamayın.**

**Şüpheli durumlarda lütfen Bilgi İşlem Daire Başkanlığı nyg.yardim@mail.ege.edu.tr adresine bilgi veriniz.**

**Ege Üniversitesi Bilgi İşlem Daire Başkanlığı, e-posta yoluyla kullanıcı ve şifre bilgisi istememektedir.**

**Lütfen hiçbir koşulda parolanızı linklere tıklayıp yazmayınız!**

**Eş Zamanlı Lokalizasyon ve Haritalama İçin Bilgisayarlı Görü ve Sensör Tabanlı Otonom Mobil Robot** başlıklı makaleniz için karar işaretlenmiştir. Karar: **Kabul Edildi**  
The decision has been marked for your article titled **Eş Zamanlı Lokalizasyon ve Haritalama İçin Bilgisayarlı Görü ve Sensör Tabanlı Otonom Mobil Robot**. Decision: **Accepted**